Check for updates

Orpiment under compression: metavalent bonding at high pressure†

Vanesa Paula Cuenca-Gotor, [ID] [a] Juan Ángel Sans, [ID] *[a] Oscar Gomis, [ID] [b] Andres Mujica,[c] Silvana Radescu,[c] Alfonso Muñoz, [ID] [c] Plácida Rodríguez-Hernández, [ID] [c] Estelina Lora da Silva, [ID] [a] Catalin Popescu, [ID] [d] Jordi Ibañez, [ID] [e] Rosario Vilaplana[b] and Francisco Javier Manjón [ID] *[a]

We report a joint experimental and theoretical study of the structural, vibrational, and electronic properties of layered monoclinic arsenic sulfide crystals (α-As$_2$S$_3$), aka mineral orpiment, under compression. X-ray diffraction and Raman scattering measurements performed on orpiment samples at high pressure and combined with *ab initio* calculations have allowed us to determine the equation of state and the tentative assignment of the symmetry of many Raman-active modes of orpiment. From our results, we conclude that no first-order phase transition occurs up to 25 GPa at room temperature; however, compression leads to an isostructural phase transition above 20 GPa. In fact, the As coordination increases from threefold at room pressure to more than fivefold above 20 GPa. This increase in coordination can be understood as the transformation from a solid with covalent bonding to a solid with metavalent bonding at high pressure, which results in a progressive decrease of the electronic and optical bandgap, an increase of the dielectric tensor components and Born effective charges, and a considerable softening of many high-frequency optical modes with increasing pressure. Moreover, we propose that the formation of metavalent bonding at high pressures may also explain the behavior of other group-15 sesquichalcogenides under compression. In fact, our results suggest that group-15 sesquichalcogenides either show metavalent bonding at room pressure or undergo a transition from p-type covalent bonding at room pressure towards metavalent bonding at high pressure, as a precursor towards metallic bonding at very high pressure.

A Introduction

Arsenic sulfide (As$_2$S$_3$) and in particular the monoclinic polymorph (α-As$_2$S$_3$), aka mineral orpiment, is one of the ores of As together with minerals realgar (α-As$_4$S$_4$) and arsenopyrite (FeAsS).[1] In particular, orpiment and realgar have been known since ancient times, with realgar being used as an orange-red pigment and orpiment as a gold-like pigment, hence its mineral name orpiment (*Aurum pigmentum* in Latin).[2] Due to the high chemical stability of

α-As$_2$S$_3$, canary yellow or King's yellow pigment was obtained from molten orpiment and has been extensively used in papyrus and objects of ancient Egypt that date back to 3.1 millennia BC.[3–5] Additionally, As$_2$S$_3$ crystals and glasses have been used as drugs to treat different illnesses, such as prophylactic diseases, asthma, tuberculosis or diabetes, and were also prescribed as antiseptics and sedatives by Aristotle and Hippocrates (IV century BC). Moreover, orpiment has been used since ancient times in traditional Chinese medicine[6] until nowadays, when arsenic sesquisulfide has proved to exhibit positive effects in cancer therapy.[7] Finally, it must be stressed that in the last decades arsenic sulfides have been investigated for different applications in photonics and non-linear optics since they possess high values of the refractive index, high IR transparency, high optical non-linearity, stability to crystallization, the possibility to be modified by femtosecond laser irradiation, and an inertness to the environment.[8,9]

As$_2$S$_3$ usually crystallizes in the monoclinic α polymorph [space group (SG) $P2_1/n$ or $P2_1/c$, No. 14];[10,11] although a triclinic dimorph of orpiment called anorpiment [SG $P\bar{1}$, No. 2] was recently discovered and approved as a new mineral by the

[a] *Instituto de Diseño para la Fabricación y Producción Automatizada, MALTA Consolider Team, Universitat Politècnica de València, 46022 Valencia, Spain. E-mail: juasant2@upv.es, fjmanjon@fis.upv.es*

[b] *Centro de Tecnologías Físicas, MALTA Consolider Team, Universitat Politècnica de València, 46022 Valencia, Spain*

[c] *Departamento de Física, Instituto de Materiales y Nanotecnología, MALTA Consolider Team, Universidad de La Laguna, 38200 San Cristóbal de La Laguna, Spain*

[d] *ALBA-CELLS, MALTA Consolider Team, 08290 Cerdanyola, Barcelona, Spain*

[e] *Institute of Earth Sciences Jaume Almera, MALTA Consolider Team, CSIC, 08028 Barcelona, Spain*

† Electronic supplementary information (ESI) available. See DOI: 10.1039/c9cp06298j
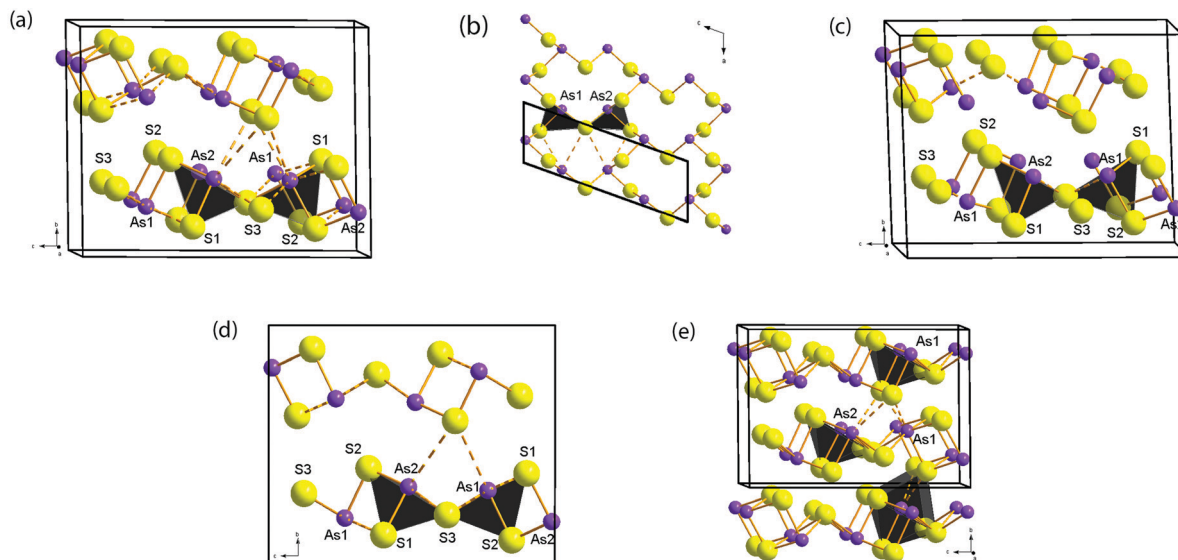
3352 | *Phys. Chem. Chem. Phys.*, 2020, **22**, 3352–3369

This journal is © the Owner Societies 2020

Fig. 1 α-As$_2$S$_3$ structure at room pressure. Big yellow and small purple spheres correspond to S and As atoms, respectively. (a) 3D structure. All solid lines correspond to bonds of similar length (~2.3 Å) and dashed lines correspond to longer As−S distances (>3.0 Å). (b) Structure of the layer in the *ac* plane showing the heart-shaped rings. The upper part shows the AsS$_3$ pyramids due to the short bonds that result in the threefold coordination of As and twofold coordination of S at room pressure. Inside the cell edges we show the long intralayer bonds that would contribute to fivefold coordination of As above 25 GPa. (c) Structure viewed as AsS spiral chains (in the As1−S1−As2−S2 sequence) joined by inter-chain S3 atoms. Only short bonds are displayed. Solid (dashed) lines correspond to intra (inter)-chain bonds. (d) Projection of the α-As$_2$S$_3$ structure onto the *bc* plane. (e) 3D structure of As$_2$S$_3$ at 30 GPa, showing polyhedral units with fivefold coordination of As1 and As2 atoms (up and middle) and with 5 + 2 coordination for As1 atoms (down).

International Mineralogical Association.[12] The crystalline structure of the monoclinic α phase (see Fig. 1) is composed of corrugated or zigzag layers piled up mainly along the *b* axis (see Fig. 1(a)), which are linked by weak van der Waals (vdW) forces.[13]

The properties of arsenic sulfides have been extensively studied, mainly for melts and glasses, because As$_2$S$_3$ ranks first among chalcogenides from the viewpoint of the production of amorphous and glass-like industrial materials. However, many properties of their crystalline phases, orpiment and anorpiment, are not yet well known, likely due to the complex monoclinic and triclinic crystalline structures of these compounds. For instance, a definitive symmetry assignment of the vibrational modes of orpiment is still under debate[14] despite a number of papers reporting Raman scattering (RS) measurements, as well as infrared (IR) measurements, since the advent of laser-based Raman spectroscopy.[14–29]

In this context, pressure is a valuable tool to study the properties of materials and several high-pressure (HP) studies have been performed on glassy As$_2$S$_3$ and α-As$_2$S$_3$ in order to help us to understand their properties. In particular, results obtained from HP optical absorption, HP X-ray absorption spectroscopy (XAS), HP-RS measurements, HP electrical measurements and from a few *ab initio* calculations have been reported for α-As$_2$S$_3$.[23,26,27,30–35] Moreover, a HP and high-temperature (HT) polymorph of orpiment (α-As$_2$S$_3$), whose structure has not been resolved yet, has been found.[34] This is not surprising because little is also known about the structure of orpiment and its behavior under compression. It is only known that the remarkable high packing of layers in orpiment is responsible for its high stability under pressure as suggested by previous experiments.

Besides, HP-XAS measurements suggested some structural changes above 10 GPa and an increase in the As coordination above 30 GPa. On the other hand, recent electrical measurements and calculations suggest an isostructural phase transition (IPT) around 25 GPa.[33]

To verify these hypotheses, it would be desirable to perform HP X-ray diffraction (XRD) measurements on α-As$_2$S$_3$ at room temperature in order to obtain the equation of state of orpiment and explore the origin of the changes proposed in the literature. Such measurements will allow us to investigate the possible appearance of HP phases and their relationship mainly with those of other sesquioxides and sesquichalcogenides. On the other hand, it will be important to perform new HP-RS measurements in order to correlate the structural and vibrational changes in orpiment and to aid in the assignment of the symmetries and the origin of the different vibrational modes with the help of *ab initio* calculations. All these measurements and calculations would allow us to understand the behavior of orpiment under compression.

For all the mentioned reasons, we report in this work a joint experimental and theoretical study of the structural, vibrational, and electronic properties of α-As$_2$S$_3$ under compression at room temperature by means of powder HP-XRD and HP-RS measurements on orpiment, where our experimental results are complemented with theoretical *ab initio* total-energy, lattice-dynamics and electronic band structure calculations.

Our structural results show continuous compression of orpiment up to 25 GPa with a large decrease of the interlayer distance, coherent with the loss of the vdW character of the dominating forces in this region. A progressive increase of the

This journal is © the Owner Societies 2020

Phys. Chem. Chem. Phys., 2020, **22**, 3352–3369 | **3353**

As coordination with compression, changing from threefold coordination at 0 GPa to more than fivefold coordination above 20 GPa, occurs as a consequence of a pressure-induced IPT around 20 GPa. Moreover, our experimental and theoretical results show a strong elastic anisotropy of orpiment layers between 0 and 23 GPa, which confirms recent results[36] and opens the door to the use of membranes of this 2D material in flexible and stretchable devices.[37,38]

Additionally, our vibrational results show a closing of the phonon gap with increasing pressure up to 16 GPa due to the large number of phonons with negative pressure coefficients (soft modes) at relatively low pressures. Our theoretical calculations have allowed us to provide a tentative symmetry assignment of the Raman-active modes in orpiment and explain their behavior under compression, which can help in identifying orpiment in ancient pigments in a non-destructive way.[39]

Our electronic band structure calculations suggest that there is a progressive closing of the bandgap of α-As_2S_3 with increasing pressure leading from a trivial semiconductor to a trivial metal well above 60 GPa, which is in very good agreement with previous optical absorption measurements[26,27,31] and suggests a possible phase transition above 42 GPa due to the recently observed metallization of orpiment.[33]

Finally, we show that all the changes observed in orpiment under compression, such as: the strong decrease of the bandgap; the softening of many optical vibrational modes; the evolution of the electron localization function (ELF) along the As–S bonds; and the strong increase of the dielectric tensor components and Born effective charges, can be explained in the framework of the formation of metavalent bonding at HP, as recently proposed for other chalcogenides.[40–45] In summary, we show in the present paper that orpiment under compression is an example, together with GeSe,[43] of a compound that develops a pressure-induced transition from covalent to metavalent bonding without the need to undergo a first-order structural phase transition. This feature contrasts with Se and Te, which undergo this change of bonding character after being the subject of a first-order phase transition. Moreover, we propose that the formation of metavalent bonding may explain the behavior under compression of other group-15 chalcogenides, so our results pave the way for extending the study of the transformation from covalent to metavalent bonding to other group-15 chalcogenides and related compounds.

B Results

B.1 Structural and vibrational characterization of α-As_2S_3 at room conditions

As already commented on, α-As_2S_3, with the monoclinic $P2_1/c$ space group at room conditions, is a layered material with corrugated (or zigzag) layers extended along the ac-plane that are linked by vdW interlayer interactions along the b-axis (Fig. 1(a)). Each corrugated layer is formed by heart-shaped six-member rings of corner-sharing AsS_3 pyramids (Fig. 1(b)) Traditionally, the zigzag layers have been understood as being formed by spiral

AsS chains extended along the a-axis and held together by inter-chain S atoms, which allow the link between the chains along the c-axis (see Fig. 1(c)). On the other hand, zigzag layers can also be seen as a W-shape formation of molecules (S1–As2–S3–As1–S2) where each molecule is linked with four adjacent inverted W-shape molecules, mostly along the c-axis due to covalent bonding (see Fig. 1(d)).

At room conditions, each As1 and As2 atom is linked by covalent bonds to one S1, one S2 and one S3 atom at distances around 2.3 Å, leading to As threefold-coordination (see the pyramids in Fig. 1(a)). Additionally, each As1 and As2 atom has two farther S neighbors in the same layer at distances above 3.0 Å (see the dashed lines inside the layers in Fig. 1(a) and (b)) and another two S neighbors in an adjacent layer at distances above 3.5 Å (see the dashed lines between the layers in the top part of Fig. 1(a) and (d)). In the following section, we will discuss the importance of these long As–S intra- and interlayer distances (above 3 Å at room pressure) in orpiment at high pressure.

According to the difference of the As–S distances, we can consider orpiment as an arrangement of AsS_3 pyramids forming AsS_3E tetrahedral units, where E refers to the lone electron pair (LEP) of the As atoms. Therefore, each layer can be described alternatively by an arrangement of two tetrahedral AsS_3E units, *i.e.* those formed by the two inequivalent As atoms, each surrounded by three S atoms and the corresponding cation LEP that points towards the interlayer space. The strong As LEP distorts the electronic distribution and the geometry of the polyhedral units leading to the layered structure of orpiment.

The layered structure of orpiment bears similarities with the chain-like structure of the valentinite mineral (β-Sb_2O_3), where the W-shape molecules (linked through a helical form) lead to the formation of an acicular or quasimolecular crystal.[46] On the other hand, the layered structure of orpiment is isostructural to that of α-As_2Se_3[47] and belongs to the same space group as the claudetite mineral (m-As_2O_3); however, claudetite is not isostructural to orpiment, because the layered structure of the former is due to the arrangement of AsO_3 molecules in a buckled structure[48] as in black phosphorous.[49] The layered structure of orpiment also bears some resemblance to the zigzag layered structure recently described for Sb_2S_3, Sb_2Se_3, and Bi_2S_3,[50–52] crystallizing in the orthorhombic *Pnma* structure, and to that of α-As_2Te_3, crystallizing in the monoclinic $C2/m$ phase.[53] In these former group-15 A_2X_3 sesquichalcogenides, the layers are clearly composed of spiral chains held together through long and weak A–X bonds, whereas in As_2S_3 the chains are connected through short and strong A–X bonds. Another difference found between these systems is regarding the cation coordination in the different structures at room pressure. In α-As_2S_3, the two inequivalent As atoms are threefold-coordinated; in Sb_2S_3, Bi_2S_3 and Sb_2Se_3, there is an average fourfold coordination because one cation has threefold coordination and the other has fivefold coordination; and in α-As_2Te_3, the As atoms have coordination between five and six. This means that the larger cation or the larger anion favors an increase of cation coordination probably due to the smaller cation LEP effect.[54]

The experimental XRD pattern of our sample at room conditions (see Fig. 2(a)) shows that the sample corresponds
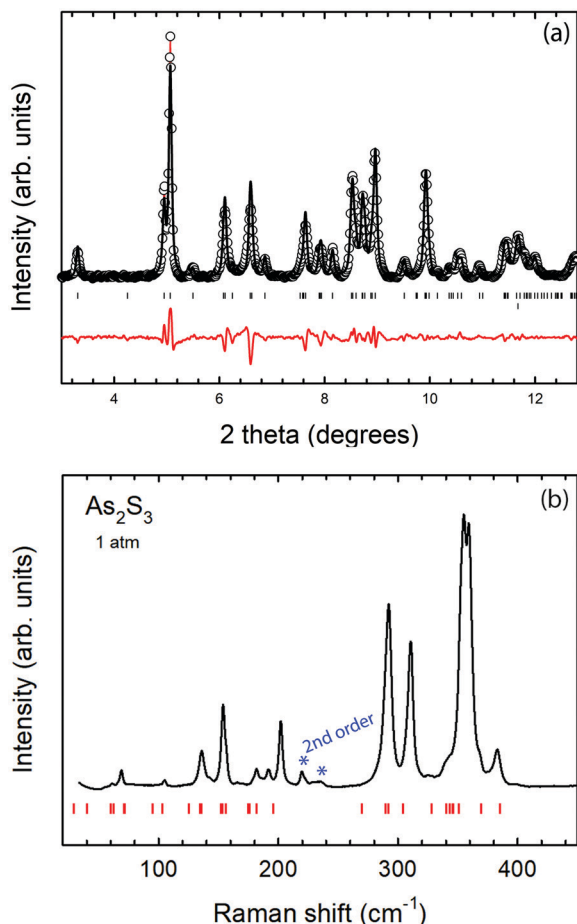
Fig. 2 Structural and vibrational characterization of α-As$_2$S$_3$ at room conditions: (a) powder XRD pattern (circles). Le Bail analysis (black solid line) and residuals (red solid line) are also plotted. (b) RS spectrum. The bottom marks indicate the theoretical Raman-active mode frequencies from calculations including vdW interactions. The asterisks indicate 2nd order Raman features.

The theoretical atomic parameters of the five inequivalent atomic sites (three S and two As atoms) of α-As$_2$S$_3$ are also given in Table S1 in the ESI,† for comparison with the experimental and theoretical values.

As regards the vibrational properties of α-As$_2$S$_3$, group theory predicts sixty vibrational modes at the Brillouin zone (BZ) center with the following mechanical representation:[56]

$$\Gamma_{60} = 15A_g\ (R) + 13B_u\ (IR) + 15B_g\ (R) + 14A_u\ (IR) + 1A_u + 2B_u$$
(1)

where g (gerade) modes are Raman-active (R) and u (ungerade) modes are infrared-active (IR), except one A_u and two B_u modes that are acoustic modes. Therefore, α-As$_2$S$_3$ has 30 Raman-active modes and 27 IR-active modes.

Fig. 2(b) shows the unpolarized RS spectrum of orpiment at room conditions together with the theoretically-predicted Raman-active mode frequencies at room pressure. The values of the experimental and theoretical frequencies of the Raman-active modes of α-As$_2$S$_3$ at room pressure are summarized in Table 2. The RS spectrum of orpiment at room pressure clearly shows 19 out of the 30 theoretically-predicted Raman-active modes and quite good agreement between our experimental and theoretical frequencies (including vdW interactions). The spectrum is similar to those previously reported, with a doublet between 60 and 70 cm^{-1}, a phonon gap between 200 and 290 cm^{-1} and a triplet around 360 cm^{-1}.[14–29,33] Unfortunately, we have not been able to observe modes below 40 cm^{-1} due to the limit imposed by the edge filter of our spectrometer.

The vibrational spectrum of orpiment at room pressure is separated between a low-frequency region (below 200 cm^{-1}) and a high-frequency region (above 260 cm^{-1}) with a phonon gap between both. Some Raman features are observed inside the phonon gap of α-As$_2$S$_3$, which are assumed to be second-order modes, so they will not be further commented on in this work. Among the measured RS modes, the more intense modes are those of the high-frequency region between 350 and 360 cm^{-1}. Due to the large number of Raman-active modes located within a small frequency region of the RS spectrum at room pressure and the broadening of experimental peaks, it is almost impossible to identify the modes by solely using the RS spectrum at room pressure and its comparison with lattice-dynamics *ab initio* calculations. Therefore, a tentative assignment of experimental peaks will be performed in a forthcoming section taking into account the HP dependence of the experimental and theoretical Raman-active mode frequencies.

to the α-phase without the presence of additional phases or impurities, within the detection limits of the technique. The pattern was fitted to a monoclinic structure ($P2_1/c$ space group), with small residuals and a correlation factor R_{wp} of 10%, yielding the following lattice parameters: $a = 4.2626(5)$ Å, $b = 9.6056(7)$ Å, $c = 12.1836(12)$ Å and $\beta = 110.054(7)°$ with $V_0 = 468.61(5)$ Å^3. In Table 1 we can observe that these values are in good agreement with previously reported experimental values,[10,11,13] with our theoretically calculated lattice parameters and with other previously published theoretical data.[33,55]

Table 1 Experimental and theoretical (with vdW) lattice parameters corresponding to the $P2_1/c$ phase of α-As$_2$S$_3$ at ambient conditions. Experimental and theoretical values from ref. 10, 11, 33 and 72 are given for comparison. All data have been expressed in the standard $P2_1/c$ setting for comparison

Lattice parameters	Experimental (this work)	Theoretical (this work)	Experimental (ref. 11)	Experimental (ref. 10)	Theoretical (ref. 33)	Theoretical (ref. 72)
a (Å)	4.2626(5)	4.2608	4.256(2)	4.22(5)	4.22	4.22
b (Å)	9.6056(7)	9.6289	9.577(5)	9.57(2)	9.65	9.57
c (Å)	12.1836(12)	12.3084	12.191 (5)	12.18(4)	12.27	12.1839
β (°)	110.054(7)	109.84	109.75(8)	109.8(5)	109.59	109.85
V_0 (Å^3)	468.61(5)	475.00	467.68	462.8	471.2	462.80

This journal is © the Owner Societies 2020

Phys. Chem. Chem. Phys., 2020, **22**, 3352–3369 | **3355**

Table 2 Theoretical (with vdW interactions) and experimental Raman-active mode frequencies and their respective pressure coefficients for α-As_2S_3 at room temperature, as fitted with equation $\omega(P) = \omega_0 + \alpha \cdot P$. Experimental values from ref. 23, 25 and 33 have been added for comparison

Mode	Theoretical		Experimental			
	$\omega_0{}^a$ (cm^{-1})	α^a (cm^{-1} GPa^{-1})	$\omega_0{}^a$ (cm^{-1})	α^a (cm^{-1} GPa^{-1})	ω_0 (cm^{-1})	α (cm^{-1} GPa^{-1})
A_g^1	27 (1)	5.1 (3)	26 (1)	6.32 (37)	25[b], 26[c]	9.0[b]
A_g^2	38 (1)	4.5 (2)	37 (1)	4.9 (3)	36[b], 37[c]	7.2[b]
A_g^3	59 (1)	4.1 (2)	62 (1)	3.7 (1)		
B_g^1	62 (1)	1.6 (2)			62[b,c]	5.0[b]
B_g^2	68 (1)	10.3 (4)	69 (3)	10.5 (8)	69[b], 70[c]	11.0[b]
A_g^4	70 (1)	5.9 (3)	70 (3)	8.1 (3)		
B_g^3	94 (2)	3.1 (1)	103 (2)	2.9 (1)		
B_g^4	103 (2)	2.1 (5)	106 (2)	2.8 (1)	107[b], 106[c]	4.9[b]
A_g^5	124 (2)	7.7 (7)	138 (5)	5.1 (4)	136[b], 137[c], 135[d]	7.3[b], -0.42[d]
B_g^5	134 (2)	0.7 (2)	120 (1)	2.9 (5)		
B_g^6	135 (2)	3.6 (1)	144 (1)	3.9 (2)	145[c]	
B_g^7	152 (3)	3.7 (2)				
A_g^6	153 (3)	-4.6 (7)	155 (2)	-0.3 (3)	158[c]	
A_g^7	155 (3)	5.5 (3)	156 (2)	6.9 (4)	154[b,c], 153[d]	8.5[b], 0.24[d]
B_g^8	174 (3)	2.5 (2)	179 (2)	2.2 (1)	180[c], 177[d]	-2.22[d]
A_g^8	176 (3)	1.2 (1)	185 (2)	2.3 (1)		
B_g^9	181 (3)	3.3 (2)	188 (2)	4.6 (9)	188[c]	
A_g^9	196 (3)	1.3 (1)	202 (1)	2.5 (2)	202[b], 204[c], 201[d]	3.2[b]
A_g^{10}	270 (4)	-3.1 (2)	291 (1)	-2.6 (3)	292[b], 293[c], 290[d]	-3.8[b], -0.89[d]
B_g^{10}	290 (4)	0.3 (1)	306 (2)	0.5 (1)	307[c], 308[d]	-0.2[d]
A_g^{11}	291 (4)	1.3 (1)	310 (2)	1.4 (1)	310[b], 312[c]	1.0[b]
B_g^{11}	305 (4)	-2.7 (1)	325 (2)	-3.5 (4)	326[b,c]	-4.6[b]
B_g^{12}	329 (5)	-3.7 (1)			343[c]	
A_g^{12}	341 (5)	1.0 (5)	356 (4)	-0.7 (6)[e]	357[b], 360[c]	0.96[b]
A_g^{13}	343 (5)	3.4 (3)	354 (4)	1.8 (4)[e]	356[c]	
B_g^{13}	345 (5)	3.1 (1)				
A_g^{14}	346 (5)	-0.5 (1)	353 (4)	4.1 (6)[e]	354[c], 353[d]	-0.19[d]
B_g^{14}	350 (5)	3.1 (4)	369 (2)	2.2 (3)	370[c]	
A_g^{15}	369 (5)	2.4 (1)	383 (2)	2.2 (2)	383[b], 384[c], 380[d]	1.7[b], 0.47[d]
B_g^{15}	385 (5)	-0.9 (2)	400 (2)	-0.7 (3)	401[c]	

^{a} This work. ^{b} Ref. 23. ^{c} Ref. 25. ^{d} Ref. 33. ^{e} The pressure coefficient of these modes has been measured above 2 GPa.

The atomic vibrations of several characteristic Raman- and IR-active modes of α-As_2S_3 have been visualized with the aid of the Jmol Interface for Crystallographic and Electronic Properties (J-ICE) interface[57] (see Fig. S1–S14 in the ESI†) and discussed in the ESI.† An interesting feature is that many vibrations evidence that atoms of the same chain (As1, S1, As2, and S2) vibrate in-phase or out-of-phase, whereas the S3 atoms interconnecting the chains vibrate in a quite different fashion than the other four inequivalent atoms. This observation clearly evidences the chain-like nature of the layers of orpiment in good agreement with a previous vibrational study.[24]

As a layered material, some of the most important vibrational modes of α-As_2S_3 are the rigid layer modes. Our calculations confirm that the two lowest-frequency modes located at 27 and 38 cm^{-1}, and attributed to the A_g^1 and A_g^2 modes, correspond to the rigid shear layer modes of orpiment (Fig. S1 in the ESI†). Moreover, our calculations show that the compressional or longitudinal rigid layer mode is the B_g^1 mode theoretically predicted at 62 cm^{-1} (Fig. S2 in the ESI†). This frequency value is in good agreement with previous estimations of the compressional mode.[22] At room pressure, we have observed that this mode is within a region where it is overlapped with inter-chain vibrational modes (see comments in the ESI†), as previously suggested.[24]

As regards other vibrational modes of orpiment, those of the high-frequency region mainly correspond to As–S stretching modes located between 350 and 400 cm^{-1} and to a mixture of As–S stretching and bending modes between 260 and 350 cm^{-1}. On the other hand, the modes located below 200 cm^{-1} correspond to pure As–S bending modes, with those below 100 cm^{-1} being mainly related to rotations and translations of the spiral chains. This result shows that spiral chains in orpiment are clearly defined rigid units. This distribution of modes agrees well with previous works that assigned the As–S bending modes and As–S stretching modes near 200 and 400 cm^{-1}, respectively.[18,58] In fact, the modes close to 380 and 350 cm^{-1} can be assigned to the antisymmetric and symmetric As–S stretching vibrations inside the spiral chains, respectively, in good agreement with previous estimations.[28]

B.2 Structural characterization of α-As_2S_3 at HP

Fig. 3 shows powder HP-XRD patterns of orpiment at selected pressures up to 26.6 GPa. The XRD patterns were analyzed by means of Le Bail fits to the monoclinic $P2_1/c$ structure, which is stable up to the maximum achievable pressure. Le Bail analysis of this material allowed the possibility of obtaining the structural parameters of α-As_2S_3 at different pressures (see Fig. 4). A progressive increase of the Bragg peak width was observed and
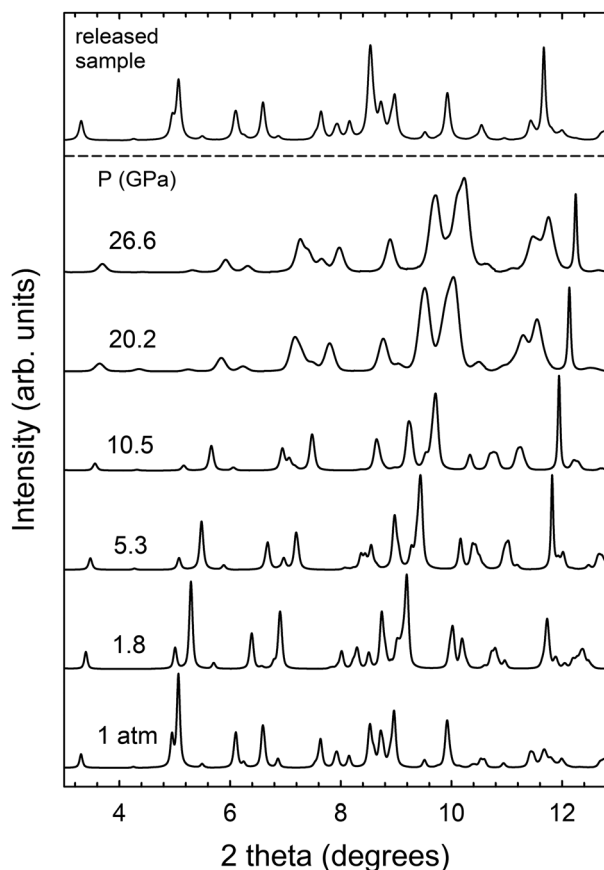
Fig. 3   Powder HP-XRD patterns of α-As$_2$S$_3$ at selected pressures up to 26.6 GPa. The patterns are shifted vertically for comparison.

Fig. 4   (a) Experimental (symbols) and theoretical (solid lines) pressure dependence of the unit-cell volume in α-As$_2$S$_3$. Black (blue) solid lines represent data from calculations including (not including) vdW interactions. The dashed lines correspond to experimental data fit with a 3rd order BM-EoS. (b) Experimental (symbols) and theoretical (solid lines) pressure dependence of the lattice parameters and monoclinic β angle (inset) in α-As$_2$S$_3$. All calculations include vdW interactions. Anorpiment EoS curve theoretically simulated is included for the sake of comparison (red solid line).

explained in the framework of a progressive loss of the hydrostatic conditions. The layered nature of this material prevents obtaining fine powder for this measurement, which led to the lack of Rietveld refinement of our XRD patterns.

A monotonous decrease of the unit-cell volume of orpiment up to 26.6 GPa is observed in Fig. 4(a), where experimental volume data at several pressures have been compared with density functional theory (DFT) calculations, both including and without including vdW interactions. At low pressures, the pressure dependence of the experimental volume agrees quite well with the theoretical simulation when vdW interactions are included. However, the experimental data above 10 GPa show a poorer agreement with these calculations and much better agreement with calculations that do not include vdW interactions. The above experimental result indicates that orpiment is more incompressible above 10 GPa, likely due to the loss of quasi-hydrostatic conditions of the pressure-transmitting medium above this pressure.

The fit of pressure vs. experimental volume up to 10 GPa through a third-order Birch–Murnaghan Equation of State (BM-EoS)[59] according to the trend shown by its F–f plot (Fig. S15 in the ESI†) yields a zero-pressure volume, bulk modulus and pressure derivative of the bulk modulus of: $V_0 = 468.61(5)$ Å^3, $B_0 = 13.3(5)$ GPa and $B_0' = 8.9(5)$, respectively. The volume at zero pressure, V_0, was fixed to the value measured outside the DAC
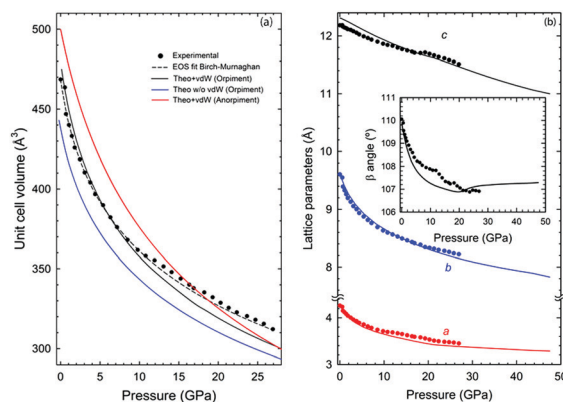
and the order of the BM-EoS was determined by the monotonously positive slope of the Eulerian strain vs. normalized pressure plot of the theoretically simulated data. This plot agrees with highly compressible non-covalent compounds with large cation LEP activity, as has been observed for structurally-related sesquichalcogenides, such as Sb$_2$S$_3$, Sb$_2$Se$_3$, Bi$_2$S$_3$ and α-As$_2$Te$_3$, characterized by bulk modulus pressure derivatives larger than 4.[52,53]

Our experimental bulk modulus and pressure derivative under hydrostatic conditions for orpiment can be compared to our theoretical data with and without vdW interactions. As expected in the description of Fig. 4(a), the theoretical bulk modulus is closer to the experimental one when the calculations include vdW interactions ($B_0 = 12.7(5)$ GPa) than when the calculations do not include them ($B_0 = 16.1(12)$ GPa). Nevertheless, the theoretical pressure derivative of the bulk modulus at zero pressure is considerably smaller than the experimental value ($B_0' = 8.9(5)$) in the case of the simulations with vdW interactions ($B_0' = 7.0(14)$) than in the simulations without vdW interactions ($B_0' = 7.9(6)$). A comparison of these results with similar compounds, such as the claudetite polymorph of As$_2$O$_3$ or α-As$_2$Te$_3$, indicates that orpiment presents a similar value of the bulk modulus to the former ($B_0 = 15.5(4)$ GPa),[60] but a much smaller value of the bulk modulus than the latter ($B_0 = 24(3)$ GPa).[53] This result is consistent with the higher LEP activity of As atoms in oxides and sulfides than in selenides and tellurides.[54]

The pressure dependence of the experimental and theoretical lattice parameters of α-As$_2$S$_3$ up to 26.6 GPa also shows a monotonous and smooth decrease (see Fig. 4(b)). The good agreement of the theoretical behavior of the volume and lattice parameters with our experimental data at room temperature allows us to conclude that no first-order phase transition occurs throughout the whole range of studied pressures. In particular, the lack of a jump in the pressure dependence of our lattice parameters and unit-cell volume in the region close to 10 GPa

This journal is © the Owner Societies 2020

Phys. Chem. Chem. Phys., 2020, 22, 3352–3369 | 3357

lead us to discard the presence of a structural phase transition in this pressure range, as was previously suggested.[30] Therefore, our results are in good agreement with recently published theoretical data.[33]

The analysis of the axial compressibility in monoclinic structures requires a more complex analysis than for more symmetric phases because the β-angle is not 90°, so the directions of maximum and minimum compressibility of the compound are usually not along any of the three crystallographic axes. Therefore, we have analyzed the compressibility of the material by calculating and diagonalizing the experimental and theoretical isothermal compressibility tensor β_{ij} at different pressures (details are given in the ESI†). This tensor is a symmetric second rank tensor that relates the state of strain of a crystal to the pressure change that induced it[61] and it has been obtained with the finite Eulerian approximation as implemented in the Win_Strain package.[62]

Fig. 5(a) and (b) describe the pressure dependence of the tensor elements (numerical data are provided in Tables S1 and S2 in the ESI†) corresponding to the compressibilities along the different axes and the direction of maximum compressibility with respect to the c-axis (ψ) or to the a-axis (θ), respectively.

According to these figures, the a-axis (the spiral axis) is more compressible than the b-axis (the axis perpendicular to the layers) up to 23 GPa. This is a surprising result for layered materials, where the axis perpendicular to the layers is usually the most compressible one; however, it is coherent with the spiral chain-like nature of the layers in orpiment and the small connectivity of the

spiral layers along the a-axis. Moreover, the compressibility of the a-axis (β_{11}) is much larger than that of the c-axis (β_{33}). This high intralayer elastic/mechanic anisotropy is consistent with that recently found in As_2S_3 nanolayers, which is similar to that of black phosphorous,[36] and certifies that orpiment layers can be potentially used in flexible, stretchable, orientation-dependent and frequency tunable electronic, optoelectronic and optomechanic devices.[37,38]

The compressibility trend among the different crystallographic directions remains constant ($\beta_{11} > \beta_{22} > \beta_{33}$) up to 23 GPa. In this pressure range, all compressibilities are positive, thus indicating a monotonous compression of the structure along the three main crystallographic axes up to 23 GPa. This result is somewhat in disagreement with previous estimates by Besson et al.,[26] who found positive and negative values for the compressibilities along the a- and c-axis of the layer plane, respectively, and suggested a compression of the layers in the direction perpendicular to the spiral chains and an expansion of the spiral chains along the helicoidal axis, similar to what occurs in trigonal Se and Te.[63,64]

The reliability of our theoretical calculations allowed us to obtain the theoretical compressibility tensor up to 32 GPa. A sudden regularization of the three axial compressibilities to roughly the same value is attained around 23 GPa, with a quick change of the direction of maximum compressibility around this pressure. At 24 GPa, the direction of maximum compressibility is found to be along the b-axis ([010] direction); this is the reason why we do not display any value in Fig. 5. However, above 27 GPa, the direction of maximum compressibility is again found to be within the ac-plane, but now it is close to the c-axis. In particular, $\Psi = 15(4)°$ and $\theta = 92(4)°$ at 32 GPa. The drastic change of the direction of the maximum compressibility observed above 23 GPa can be considered as a more significant feature of the variation of properties associated with the low-pressure structure.

For completeness, the experimental and theoretical pressure dependence of the axial ratios in α-As_2S_3 are shown in Fig. S16 in the ESI.† The monotonous trend of all the axial ratios is well reproduced by our theoretical calculations including vdW interactions. A closer look into the slopes reveals a clear change of tendency above 20 GPa, where all three ratios seem to become insensitive to pressure up to 50 GPa. A similar behavior is observed in the pressure dependence of the β-angle (inset of Fig. 4(b)). In some previous studies, the change in the axial ratios of several group-15 sesquichalcogenides has been considered as proof of the occurrence of a pressure-induced electronic topological transition (ETT),[50,65,66] since a minimum of the c/a ratio has previously been observed to be coincident with the occurrence of a pressure-induced ETT in α-Bi_2Se_3, α-Sb_2Te_3, and α-Bi_2Te_3.[67] However, in a recent work,[52,68] this fact has been put into question because the minimum of the c/a ratio can simply originate from a change of the ratio of interlayer/intralayer forces in layered materials. The change of the minimum of the c/a ratio does not necessarily warrant a change in the electronic density of states near the Fermi level leading to an ETT; however, it can be indicative of an IPT, as recently suggested for orpiment.[33]
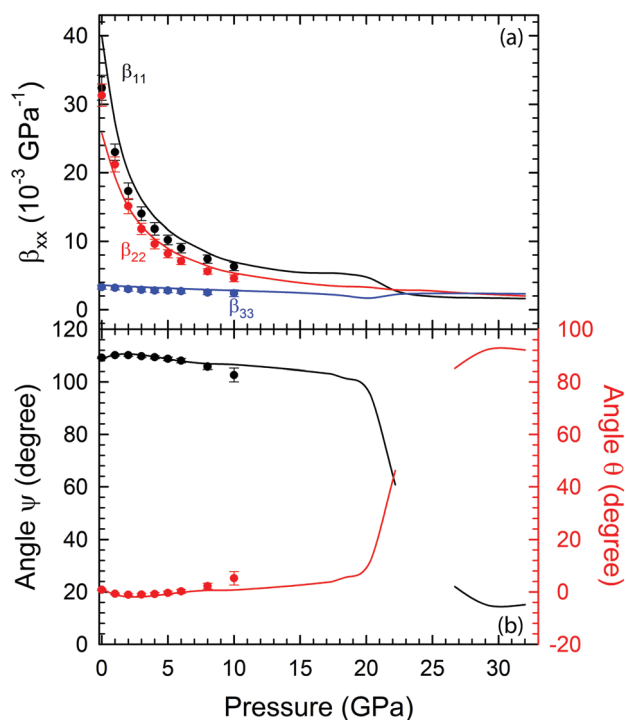

Fig. 5 (a) β_{xx} coefficients of the compressibility tensor that indicates the compressibility along the different crystallographic axes. (b) Angle of maximum compressibility ψ relative to the c-axis (from c to a) or equivalently θ relative to the a-axis (from a to c). Solid lines represent data from calculations and symbols data from our experiments.

3358 | Phys. Chem. Chem. Phys., 2020, 22, 3352–3369

This journal is © the Owner Societies 2020

To prove that the change of the axial ratios is indicative of a pressure-induced IPT, we have analyzed the pressure dependence of the internal atomic parameters of the five inequivalent atomic sites in α-As$_2$S$_3$ (see Fig. S17 in the ESI†). The most noticeable results are those observed for the three coordinates of the two inequivalent As atoms, which show a clear trend towards certain fixed coordinates above 18(25) GPa, as obtained for calculations without (with) vdW interactions. This result occurs at similar pressures at which the change of the direction of the maximum compressibility was observed. This result clearly indicates a modification of the HP behavior of the low-pressure phase.

A remarkable result, derived from the pressure dependence of the atomic coordinates, is the grouping and regularization of many theoretical As–S interatomic distances around 18 (25) GPa, without (with) vdW interactions (see Fig. 6). As a consequence, there is an increase of As1 coordination from threefold at 0 GPa to more than fivefold (5 + 2) above 20 GPa (see Fig. 1e) because, on one hand, all As1–S1 and As1–S3 intralayer distances become similar, thus giving fivefold coordination and, on the other hand, two additional As1–S2 interlayer distances become smaller than 3 Å. Similarly, there is an increase of As2 coordination from threefold at 0 GPa to fivefold above 20 GPa that stems from the equalization of the As2–S2 and As2–S3 intralayer distances. In summary, we can conclude that above 20 GPa the As1 (As2) polyhedral units of orpiment pass from threefold coordination

towards sevenfold (fivefold) coordination without changing the space group.

A more detailed analysis of the As polyhedral units (see Fig. S18–S20 in the ESI†) shows how both As1 and As2 polyhedral units remain in threefold effective coordination below 10 GPa. However, above this critical pressure, there is a progressive increase of the effective coordination up to 22 GPa, where the As2 polyhedron remains in fivefold effective coordination, whereas the As1 polyhedral unit increases up to sixfold effective coordination (Fig. S20 in the ESI†). We must note that in distorted polyhedral units (values very different from 0 in Fig. S19 in the ESI†), the effective coordination number does not describe properly the coordination of the polyhedral unit because some of the interatomic distances are longer than others, thus leading to effective coordination dominated by the next neighbors (Fig. S20 in the ESI†) but with large polyhedral volumes (Fig. S18 in the ESI†). Above 20 GPa, the effective coordination of As1 is slightly larger than five despite the real coordination is higher (5 + 2). The reason for the discrepancy is the strong distortion of the polyhedral unit around As1, whereas for As2 the effective coordination (five) coincides with the real coordination due to the proximity of the interatomic distances.

The above results between 0 and 20 GPa are consistent with: (i) the regularization of the axial compressibilities, (ii) the trend towards fixed As coordinates found, and (iii) the similar x and z
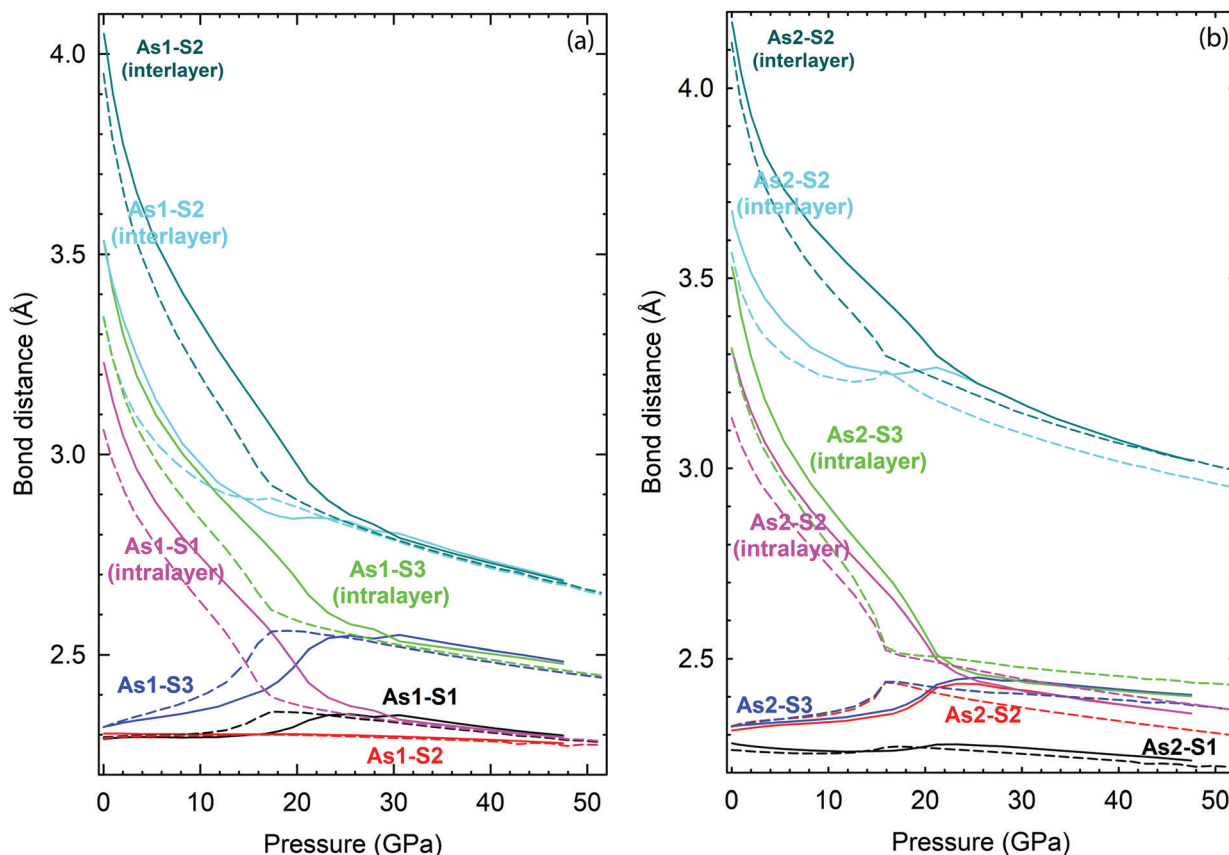

Fig. 6 Evolution under pressure of the theoretical As–S interatomic distances of α-As$_2$S$_3$. (a) As1 and its next-neighbor S atoms. (b) As2 and its next-neighbor S atoms. Solid (dashed) lines represent data from theoretical calculations that include (do not include) vdW interactions.

This journal is © the Owner Societies 2020

Phys. Chem. Chem. Phys., 2020, 22, 3352–3369 | 3359

coordinates shown by the Wyckoff sites of As1, S2, and S3 atoms above 18(25) GPa in our calculations without (with) vdW interactions. All these results indicate the presence of an IPT above 20 GPa, in agreement with a recent paper[33] and also with HP-XAS results that reported a change in the As environment above 10 GPa and an increase of As coordination above 30 GPa.[30]

In summary, HP-XRD measurements and DFT calculations carried out up to 32 GPa show that the effect of pressure upon the structure of α-As_2S_3 does not result in a first-order phase transition, but triggers a change of the trend of atomic coordinates and of axial ratios, and an increase of the coordination of As atoms above 20 GPa, as well as a drastic change of the direction of the maximum compressibility above 23 GPa. All these features are in good agreement with published data[30,33] and could be attributed to a pressure-induced IPT in orpiment above 20 GPa.

B.3 Vibrational characterization of α-As_2S_3 at HP

In order to study the effect of pressure on the vibrational properties of orpiment and better understand the HP behavior of α-As_2S_3, we have carried out HP-RS measurements on orpiment samples up to 14.5 GPa. The experimental results are compared to lattice-dynamics calculations of α-As_2S_3. In Fig. 7 we show the room-temperature RS spectra of orpiment at selected pressures under hydrostatic conditions. In this figure, the absence of any
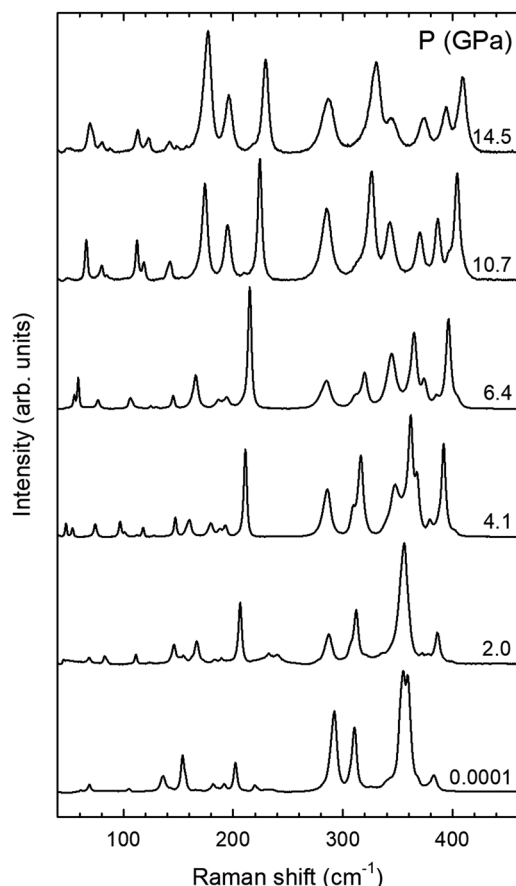

Fig. 7 Room-temperature RS spectra of orpiment at selected pressures up to 15 GPa.

first-order PT in orpiment up to 14.5 GPa is clearly observed, in good agreement with our HP-XRD measurements and previously published results.[30,33] However, the RS spectra show a much larger number of Raman modes between 2.0 and 4.1 GPa, despite the disappearance of the Raman modes in the phonon gap between 210 and 250 cm^{-1}. As already commented on, these modes in the phonon gap, together with a mode observed above 1 GPa near 120 cm^{-1}, are assumed to be second-order modes and will not be further discussed. No major changes of the RS spectra are observed between 4.1 and 14.5 GPa. In this context, it must be noted that the bandgap of orpiment (2.7 eV at room pressure) decreases under pressure at a rate of -0.14 eV GPa^{-1}.[26,31] This means that the bandgap equals the HeNe laser energy (1.96 eV) at 5.3 GPa, so some resonance effects could be observed above *ca.* 4 GPa. However, there is no damage in the sample or redshift of frequency modes after long exposure time to the laser, which indicates the lack of radiation damage in our samples.

As already mentioned, it is very difficult to assign the features that show up in the room-pressure RS spectrum of α-As_2S_3. However, it is possible to perform a tentative peak assignment by studying the pressure dependence of the Raman-active modes in combination with lattice-dynamics calculations on the basis of the correlation of the frequencies and their pressure coefficients (see Table 2 and Fig. 8(a)). Our observed frequencies and pressure coefficients are in good agreement with previous HP-RS studies.[23,26,27,33] Notably, the shear or transverse rigid modes A_g^1 and A_g^2 at 26 and 37 cm^{-1} and the first B_g mode (B_g^2 mode) at 69 cm^{-1} show the largest relative increase of frequency under compression (0.24, 0.13 and 0.15 GPa^{-1}, respectively). Moreover, the B_g^2 mode shows the experimental and theoretical largest pressure coefficient and mode Grüneisen parameter of all Raman-active modes (around 10.5 cm^{-1} GPa^{-1} and 1.97, respectively).

While the above results regarding the shear rigid layer A_g modes are rather common in layered materials, the result regarding the B_g^2 mode is quite surprising because the largest pressure coefficient is indeed expected for the compressional or longitudinal layer mode B_g^1 located at 62 cm^{-1} (see Fig. S2 in the ESI†). It is well known that the compressional layer mode usually shows higher frequencies and pressure coefficients than those of the shear rigid layer modes in layered materials with vdW interactions between the layers. This common trend is due to the extraordinary increase of the stretching force constant between neighboring layers caused by the strong decrease of the interlayer distance, as discussed in a recent paper.[69] However, we have found that the B_g^1 mode in orpiment (not observed experimentally) shows a rather small theoretical pressure coefficient (see Table 2). This anomalous pressure dependence of the compressional mode of orpiment can be understood by considering a frequency anticrossing (occurring already at room pressure) between the B_g^1 and B_g^2 modes. In fact, the large pressure coefficient of the "bare" B_g^1 mode (see the dashed line in Fig. 8(b)) is so large when compared to the other Raman modes that this mode undergoes anticrossings with up to four B_g modes (up to B_g^5) in the pressure range between 0 and 15 GPa. This anticrossing allows us to explain the small pressure coefficient of the B_g^1 mode and the large pressure

3360 | *Phys. Chem. Chem. Phys.*, 2020, **22**, 3352–3369
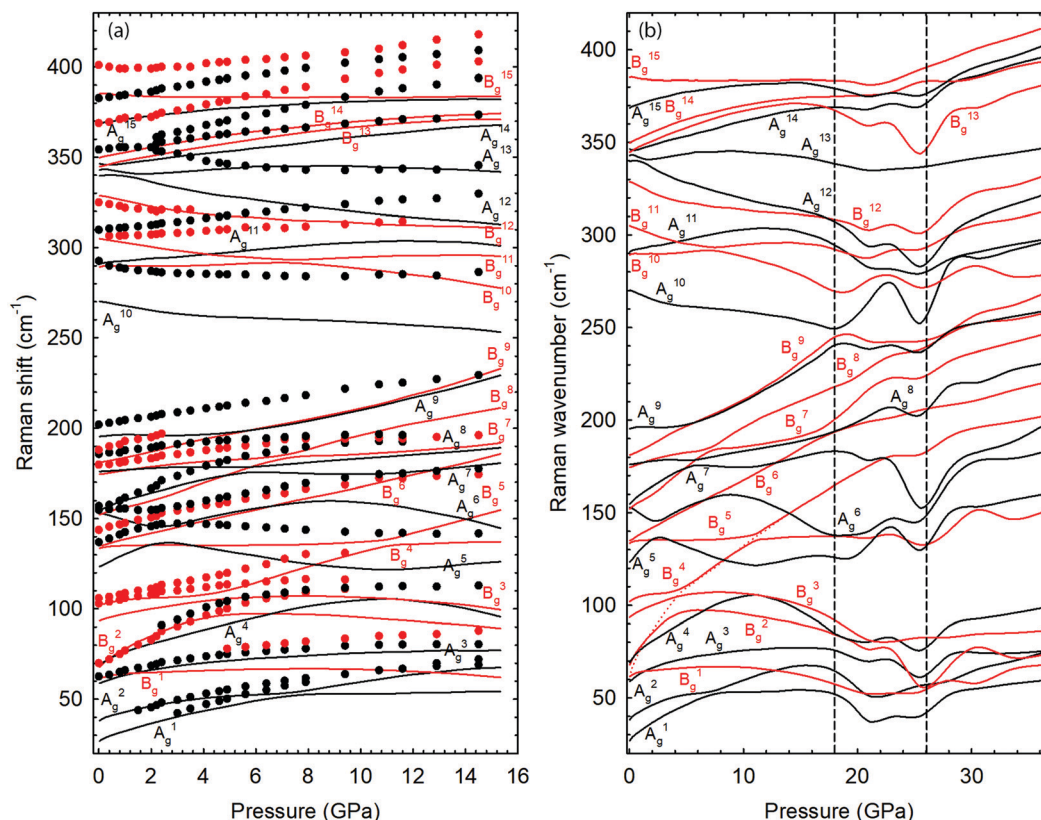
This journal is © the Owner Societies 2020

Fig. 8 (a) Experimental (symbols) and theoretical (lines) pressure dependence of the Raman-active mode frequencies of As_2S_3 up to 16 GPa. The black (red) color represents A_g (B_g) Raman-active modes. Theoretical curves correspond to calculations with vdW interactions. (b) Pressure dependence of the theoretical Raman-active mode frequencies of As_2S_3 up to 36 GPa. The red dotted line represents the tentative pressure dependence of the "bare" B_g^1 mode (the compressional rigid layer mode) if no anticrossing would occur with other modes of the same symmetry. Note that a change in the pressure coefficient of the "bare" B_g^1 mode is observed near 4 GPa and that a considerable softening of some vibrational modes is observed between 18 and 26 GPa.

coefficient of the B_g^2 mode of orpiment. Moreover, this puzzling behavior may explain why the compressional mode was not previously assigned, despite the frequency of the compressional mode was well identified in a previous work[22] as well as the pressure coefficient of the B_g^2 mode.[23]

As observed in Fig. 8(a), the experimental and theoretical frequencies of the Raman-active modes do not show a simple monotonic behavior with increasing pressure. In fact, many Raman modes exhibit a complex behavior under pressure with crossings and anticrossings of modes with different and equal symmetries, respectively. This complex behavior stems from the presence of 30 Raman-active modes in a small frequency region between 30 and 400 cm^{-1}, similarly to what has been found in monoclinic α-As_2Te_3.[53] Despite the complex behavior observed in our theoretical Raman-active modes, several experimental modes have shown a behavior consistent with the theoretical modes. In particular, we have found an experimental reduction of the phonon gap with pressure, an anticrossing of Raman modes close to 150 cm^{-1} around 2 GPa, and the splitting of several Raman modes located near 350 cm^{-1}, which are in good agreement with previous results.[26,27,33] Such behaviors are supported by our lattice-dynamics calculations for the pressure dependence of the A_g^9 and A_g^{10} modes, the A_g^5 and A_g^6 modes and the A_g^{12}, A_g^{13} and A_g^{14} modes, respectively (see Fig. 8(a)).

A striking feature of orpiment is the large number of Raman modes with negative pressure coefficients at room pressure. This is confirmed by both experimental and theoretical data. In particular, the modes located at 155, 291, 325, 356 and 400 cm^{-1} show softening under pressure in rather good agreement with previous measurements.[23,33] As noted by Besson et al.,[26] negative pressure coefficients of internal modes have been observed in Raman measurements of other chain-like structures, such as trigonal S, Se and Te,[70–72] but never for ring molecules, like those found in orthorhombic S.[23] In trigonal S, Se and Te, the soft Raman phonon is the A_1 mode (the breathing mode of the chains in the ab-plane[73]) and it can be related to the expansion of the c-axis, caused by the increase of the Se–Se intra-chain distance, at the expense of the contraction of the a-axis, caused by the decrease of the Se–Se inter-chain distance. In orpiment, the situation is quite different because all three a-, b-, and c-axes suffer a contraction under compression so the explanation for the negative pressure coefficients is not related to the elongation of any axis.

Fig. 6 shows that the As1–S3, As2–S2, and As2–S3 (As1–S1) intralayer distances increase above 0(10) GPa, thus providing an explanation for the softening of several phonons in different pressure ranges. Notably, changes of the pressure coefficient of some experimental and theoretical Raman-active modes have

This journal is © the Owner Societies 2020

Phys. Chem. Chem. Phys., 2020, 22, 3352–3369 | 3361

been observed around 4 GPa in α-As$_2$S$_3$, which could be attributed to the strong changes of the interatomic distances around these pressures. The changes can be clearly observed in the experimental B$_g^1$ and A$_g^{10}$ modes and in the theoretical A$_g^2$, B$_g^1$, A$_g^8$, A$_g^9$, A$_g^{10}$ and A$_g^{15}$ modes (see Fig. 8(a)). They can also be observed in the theoretical B$_u^1$, A$_u^2$, A$_u^3$, A$_u^8$, B$_u^7$, B$_u^8$ and A$_u^9$ modes (see Fig. S21 in the ESI†), which do not evidence anticrossings between 0 and 6 GPa.

Fig. 8(b) and Fig. S21 (ESI†) show a notable softening of the theoretical vibrational modes of orpiment in the region between 18 and 26 GPa, where the pressure-induced IPT occurs according to our calculations. In order to probe the possibility of a second-order IPT occurring in α-As$_2$S$_3$, we have studied the phonon dispersion curves calculated at different pressure values, ranging up to 30 GPa (see Fig. S22 and S23 in the ESI†), because a second-order IPT is related to the presence of a soft phonon mode according to Landau theory. Since we do not observe any soft mode up to 30 GPa, we can conclude that the pressure-induced IPT occurring in α-As$_2$S$_3$ above 20 GPa must be of order higher than 2, *i.e.* an IPT of electronic origin, such as the pressure-induced ETTs observed in other group-15 sesquichalcogenides.[67]

In summary, HP-RS measurements and lattice-dynamics calculations on orpiment carried out up to 37 GPa show that the lattice-dynamics of orpiment at HP is quite complex and has a large number of optical modes with negative pressure coefficients, related to the increase of some As–S bond distances, which cause a decrease of the phonon gap in orpiment under compression up to 20 GPa. Above this pressure, most phonons show a positive pressure coefficient, thus showing a complete change in the behavior of the phonons of orpiment below and above 20 GPa; however, no soft modes going to zero frequency have been observed according to Landau theory so we can conclude that the IPT near 20 GPa is not of second-order but of higher order, *i.e.* of electronic origin. Moreover, we have provided a tentative assignment of the Raman- and IR-active modes that can help in studying orpiment in ancient artworks using non-destructive techniques such as Raman and IR spectroscopy.[39]

B.4 Electronic band structure calculations of α-As$_2$S$_3$ at HP

To complete the picture of the behavior of orpiment at HP and in order to assess whether a pressure-induced ETT could be observed in orpiment, we have performed *ab initio* electronic band-structure calculations of α-As$_2$S$_3$ at different pressures to identify possible changes of the band extrema that could be related to a pressure-induced ETT (see Fig. 9). Our calculations show that orpiment is an indirect bandgap (1.7 eV) semiconductor at 0 GPa, with the valence band maximum (VBM) and conduction band minimum (CBM) being located along the high-symmetry segment of the Y–Γ and Γ–Z directions, respectively. The value of the bandgap is clearly underestimated by our DFT calculations, since orpiment is known to have a bandgap around 2.7 eV at room pressure,[26,31] but the structure of the electronic bands and the bandgap evolution with pressure are correctly described by this method. The bandgap energy value in our calculations is similar to the values reported by
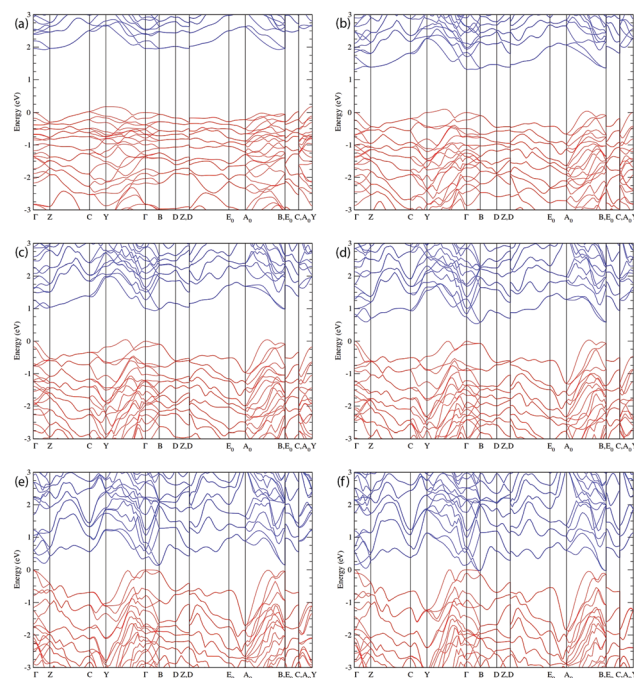

Fig. 9 Calculated band structure of As$_2$S$_3$ at different pressures: (a) 0 GPa, (b) 5 GPa, (c) 10 GPa, (d) 15 GPa, (e) 20 GPa, and (f) 30 GPa.

recent *ab initio* calculations, however differing in the precise locations of the VBM and CBM.[33,55]

There are considerable changes in the VBM and CBM of α-As$_2$S$_3$ at HP. Both the valence and conduction bands show low dispersion across the BZ at 0 GPa, but high dispersion above 20 GPa. The flat bands at 0 GPa reflect the 2D character of orpiment, while the highly-dispersed bands above 20 GPa reflect the 3D character of orpiment above this pressure. It can be observed that above 20 GPa, the VBM shifts to the Γ-point and along the Γ–B direction, whereas the CBM moves to the B-point. Additionally, a variation of the VBM occurs between 20 and 30 GPa, with the VBM at 30 GPa shifted along the high-symmetry Γ–Y direction. Since we observe the crossing of an extremum through the Fermi level above 20 GPa, thus modifying the topology of the Fermi-surface, we thus suggest a possible pressure-induced ETT above this pressure in α-As$_2$S$_3$.

The calculated indirect bandgap exhibits a strong decrease at HP from 1.7 eV at 0 GPa to 0 eV at 26 GPa (see the solid line in Fig. 10). Therefore, our calculations provide evidence for a semiconducting–metallic transition in orpiment above 26 GPa. A recent experiment suggests that metallization in orpiment should occur above 42 GPa.[33] If we assume that metallization occurs in the monoclinic $P2_1/n$ phase around 42 GPa, the underestimation of the bandgap by our DFT calculations would be only 0.3 eV (see the long dashed line in Fig. 10); however, if we take into account the value of the experimental bandgap at room pressure (2.7 eV), *i.e.* assuming an underestimation of the bandgap of 1.0 eV, and shift the calculated bandgap to match the latter, the evolution of the bandgap (see the short dashed line in Fig. 10) agrees remarkably well with the behavior of the optical bandgap (symbols in Fig. 10).[26,27] In fact, the decrease of the
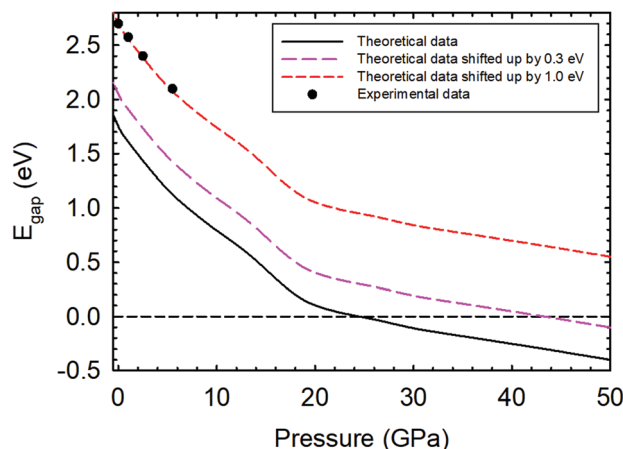
Fig. 10 Pressure dependence of the energy bandgap of orpiment. Solid, long dashed and short dashed lines correspond to results of theoretical calculations including vdW interactions, theoretical calculations shifted by 0.3 eV (to match the metallization observed above 42 GPa in ref. 33) and theoretical calculations shifted by 1.0 eV (to match the optical bandgap at 0 GPa as in ref. 26 and 27), respectively. Symbols correspond to experimental data from ref. 26 and 27.

electronic bandgap shows a theoretical pressure coefficient of -0.16 eV GPa^{-1}, which is in very good agreement with a previous experimental estimation of the optical bandgap pressure coefficient (-0.14 eV GPa^{-1}).[26,27,31] Assuming the 1.0 eV bandgap underestimation of our calculations, the extrapolation of the shifted calculated bandgap to 0 eV yields a closure of the bandgap of the monoclinic $P2_1/n$ phase at pressures that go beyond the studied range (above 50 GPa). This result suggests that the observed metallization at 42 GPa[33] could be explained by the non-hydrostatic conditions in the sample during electric measurements or by a phase transition towards another phase. In this context, we have found a triclinic $P\bar{1}$ phase that is energetically more favorable than the $P2_1/n$ phase above 40 GPa (see the enthalpy vs. pressure plot in Fig. S24, ESI†). This result suggests that the existence of a phase transition towards a metallic phase of As_2S_3 above 40 GPa is possible in good agreement with ref. 33.

In summary, our calculations show that α-As_2S_3 is a semiconductor with an indirect bandgap (~ 2.7 eV at room pressure) that decreases at HP at an initial rate of ~ -0.16 eV GPa^{-1} and becomes a metal well above 50 GPa. These features are in perfect agreement with already reported optical absorption measurements. Besides, we observe a clear change in the VBM above 20 GPa that could lead to a pressure-induced ETT, i.e. an IPT of order $2^{1/2}$ according to Ehrenfest notation.[74] Furthermore, we propose that there could be a possible first-order phase transition in orpiment above 40 GPa to a metallic phase that would explain the recent results on HP electrical measurements.[33]

B.5 Metavalent bonding in α-As_2S_3

In this section, we will show that the results obtained so far for the pressure dependence of the structural, vibrational, optical and electric properties of α-As_2S_3 can be understood in the light of a special case of resonant bonding formalism.[40–45] This bonding has recently been termed as metavalent bonding in

order to distinguish it from the resonant bonding occurring in benzene and graphite.[44] In particular, we will show that the HP behavior of orpiment between 0 and 20 GPa can be considered as the process of change from p-type covalent bonding towards metavalent bonding at HP. Moreover, we will show that the concept of metavalent bonding could be extended to understand the pressure behavior of other group-15 sesquichalcogenides and of trigonal Se and Te.

Metavalent bonding is a recently proposed new class of bonding formalism, mainly located between p-type covalent bonding and metallic bonding, which is characteristic of a new type of materials termed "incipient metals".[44] This kind of bonding occurs in materials where there is a deficiency of valence electrons in the unit cell, forming a large number of bonds, such as in octahedrally-coordinated rocksalt-related structures like those found in GeTe, SnTe, PbSe, PbTe, Sb, Bi, Sb_2Te_3, Bi_2Se_3, Bi_2Te_3, $AgSbTe_2$, $AgBiSe_2$, $AgBiTe_2$, and $GeSb_2Te_4$.[41,44,45] Under these circumstances, the few valence electrons available in the formula unit must be shared (resonate) between several bonds in order to provide the most symmetrical structure, i.e. with the largest number of similar bonds and with the largest possible cation coordination (highest packing), compatible with the valence electrons available and strain limitations, e.g. those imposed by stereoactive LEPs.[75–77]

The main characteristics of metavalent bonding are: (i) cation coordination much higher than that assumed with the 8-N rule; (ii) high Born effective charges that are much larger than the valence of the atoms; (iii) higher optical dielectric constants than typical covalent materials; (iv) high mode Grüneisen parameters of phonons and lower wavenumbers of optical phonons than typical covalent materials, thus revealing a high lattice anharmonicity causing a very small thermal conductivity; and (v) a moderately high electrical conductivity caused by a very small bandgap. All these features stem from the partial delocalization of electrons that are shared between several bonds. Due to these characteristics, materials featuring metavalent bonding have been named "incipient metals" because they show characteristics close to those of metals. In fact, they exhibit extraordinary properties that make them ideal candidates for phase-change materials, thermoelectric materials, and topological insulators.

Regarding orpiment, the equalization of the As–S intralayer distances above 18(25) GPa according to our calculations without (with) considering vdW interactions is in agreement with the bonding variation nature of As–S bonds from covalent to metavalent.[43–45] To prove such a fact, we have probed the bonding character of orpiment at different pressures, e.g. the electron localization function (ELF) along the seven next-neighbor As–S distances, the dielectric tensor, and the Born effective charges, as suggested in ref. 44.

The increase of the metavalent bonding in orpiment under compression can be traced by the increase of the theoretical dielectric constants and the Born effective charges (see Fig. 11), as commented on in ref. 40 and 44. A strong increase in the absolute value of most of these magnitudes is observed between 0 and 20 GPa.[78] The only Born effective charge component that does not show similar behavior within the range of 0 and 20 GPa

This journal is © the Owner Societies 2020

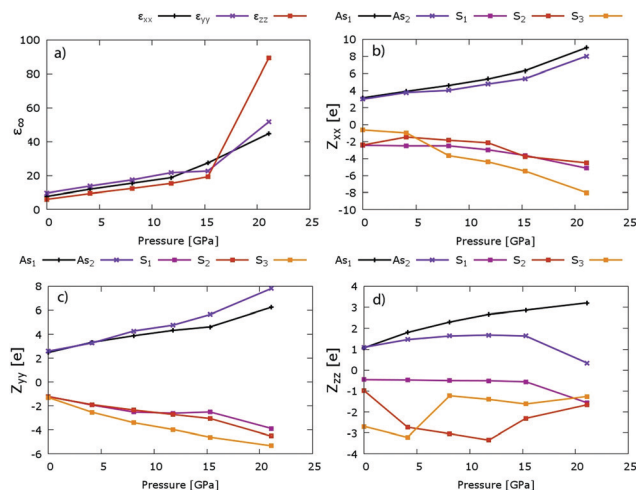Phys. Chem. Chem. Phys., 2020, **22**, 3352–3369 | **3363**

Fig. 11 Pressure dependence of the static dielectric function along the main crystallographic axes (a) and Born effective charges of the different As1, As2, S1, S2 and S3 atoms along the main crystallographic axes (b–d).

is the Z_{zz} component, which is related to the c-axis, the direction of the smallest change in bonding character because it is the direction of smaller compressibility (see Fig. 5). These changes are a clear indication of the decrease (increase) of the covalent (metavalent) bonding of the layers of orpiment. Besides, the strong decrease of the optical bandgap with pressure and the metallization of orpiment well above 50 GPa are consistent with the metavalent bonding observed for chalcogenides.[44,45] The rapid delocalization of the electron charge density over the plane of the layers caused by the steep increase of coordination of As atoms due to the strong compression of the chains mainly along the a-axis is the origin of the pronounced negative slope of the bandgap with increasing pressure.

Similarly to what was done with GeSe to study the pressure dependence of the Ge–Se bonds,[43] we plot in Fig. 12 the ELF values along the seven next-neighbor As1–S and As2–S distances obtained from our theoretical results at 0 and 25 GPa. At 0 GPa, both the As1 and As2 atoms have high ELF values (around 0.8) close to the center of the As–S bonds for each of

Fig. 12 Pressure dependence of the ELF along the As1–S (top) and As2–S (bottom) bonds at 0 GPa (a) and 25 GPa (b).

the three bonds of each As atom (As1–S1, As1–S2, As1–S3, As2–S1, As2–S2, and As2–S3), thus evidencing the threefold coordination of As1 and As2 atoms and the covalent bonding in orpiment at room pressure. However, at 25 GPa there are five intralayer As2–S bonds with high ELF values (an As2–S1 bond above 0.8 and two As2–S2 and two As2–S3 bonds above 0.6) showing fivefold coordination for As2 in orpiment. A similar situation occurs for the As1 atoms at 25 GPa, with five intralayer As1–S bonds with a relatively high ELF (an As1–S2 bond near 0.8, two As1–S1 above 0.7 and two As1–S3 above 0.5), but also with two interlayer As1–S2 bonds with an intermediate value of the ELF (slightly above 0.2), which can be considered to support 5 + 2 coordination. Note that the typical metavalent bonding in the layer plane (ac-plane) of orpiment is clear for the As2 atoms, where all four intralayer bonds (As2–S2, As2–S3, As2–S4, and As2–S5) have the same ELF value because they have the same As2–S length. On the other hand, the character of the As1–S bonds is more complex because the ELF values and lengths of all the intralayer bonds are not equal. Such behavior suggests that the intralayer metavalent bonding of As1 atoms is sacrificed by a larger coordination number taking into account the S atoms of adjacent layers. Note that these S atoms are not linked to the As2 atoms of the monoclinic structure even up to 50 GPa, what evidences the different behavior of As1 and As2 atoms on increasing pressure. The larger coordination of As1 atoms at HP is indicative of a tendency of As1 atoms towards metallic bonding, which is usually characterized by a much larger effective coordination number than covalent and metavalent bonding.[44,45]

The decrease of the bond force (ELF value) of some As–S bonds in orpiment is likely related to the length increase of those bonds (see Fig. 6), because the charge of valence electrons in As atoms must progressively be redistributed among several equidistant As–S bonds within the context of metavalent bonding.[44,45] Therefore, the charge at each of the short bonds at low pressure is redistributed between two equal bonds at HP leading to a smaller ELF for the initial short bonds at HP than room pressure. Such a feature is confirmed by the equal values of the ELF in As–S bonds of equal length at HP already commented on. Therefore, the decrease of the ELF of the original covalent bonds at HP clearly shows the delocalization of electronic charge in these bonds to form metavalent bonds at HP.

This bond enlargement and charge redistribution typical of the formation of metavalent bonds are expected to cause a decrease of some of the optical phonon frequencies. In particular, a softening of the transverse optical (TO) and longitudinal optical (LO) modes has been predicted in rocksalt compounds with metavalent bonding as compared to the same compound in the absence of metavalent bonding.[41,42] For a monoclinic compound, such as orpiment, the situation is more complex, because the TO and LO modes of the rocksalt structure are split into many components due to the decrease in symmetry. Therefore, we expect that many optical modes of orpiment will soften with increasing pressure due to the establishment of long-range interactions between neighboring atoms upon increasing the metavalent bonding at increasing pressure. In fact, Table 2 and Fig. 8 show that one of the most characteristic modes that exhibit a negative
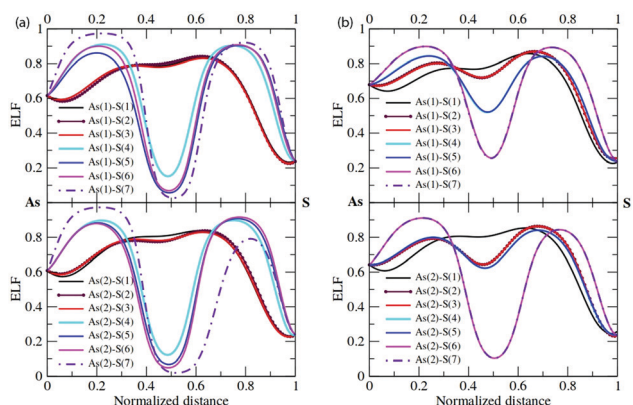
pressure coefficient is the A_g^{10} mode (see atomic vibrations in Fig. S11 in the ESI†), which is experimentally observed at 291 cm^{-1} at room pressure. Other soft Raman- and IR-active modes can be observed in Fig. 8(b) and Fig. S21 in the ESI,† respectively. Moreover, these last figures show a clear decrease of the phonon bandgap (between A_g^9 and A_g^{10} and between B_u^7 and B_u^8) from 0 to 20 GPa. This decrease of the phonon bandgap is also expected in the context of metavalent bonding.[41,42,44] Finally, we observed a considerable softening of several modes taking place between 18 and 26 GPa and clear positive slopes of most vibrational modes above 26 GPa, *i.e.* once the bonding transition to metavalent bonding takes over. These features are in agreement with the development of metavalent bonding since low-frequency values of optical vibrational modes and positive slopes of all Raman-active and IR-active modes have been observed in Bi$_2$Se$_3$, Sb$_2$Te$_3$ and Bi$_2$Te$_3$, which are metavalent compounds at room pressure.[67]

A closer look into the HP behavior of other chalcogenides evidences that the softening of optical modes at HP has been observed in a number of chalcogenides, thus suggesting that metavalent bonding is more common than expected at HP in these compounds. Several modes of the low-pressure trigonal phase of Se and Te exhibit a pronounced softening at HP. However, no softening has been found in the HP phases of these two elements,[79,80] as happens in Bi$_2$Se$_3$, Bi$_2$Te$_3$ and Sb$_2$Te$_3$.[67] This result is consistent with the recent confirmation of the metavalent bonding in Bi$_2$Se$_3$, Bi$_2$Te$_3$ and Sb$_2$Te$_3$ and β-As$_2$Te$_3$ at room conditions[81] and with the formation of metavalent bonding in Se and Te at HP.[44] Therefore, we expect a similar increase of dielectric constants and Born effective charges at HP in the low-pressure trigonal phase of Se and Te, as has been shown in orpiment and other compounds.[40,44,45]

Finally, we want to emphasize that the analysis of the different group-15 sesquichalcogenides (Table S3 in the ESI†) reveals that their behavior at HP can also be understood in the framework of metavalent bonding. In particular, some of these materials possess metavalent bonding at room pressure[81] and our work shows that some others tend to metavalent bonding at HP. For instance, a similar situation to that of α-As$_2$S$_3$ is expected to occur for isostructural α-As$_2$Se$_3$ and for β-As$_2$Se$_3$ at HP since both compounds feature threefold coordination at room pressure. Unfortunately, there are almost no HP studies of these compounds. On the other hand, α-Sb$_2$S$_3$, α-Sb$_2$Se$_3$ and α-Bi$_2$S$_3$, which crystallize in the orthorhombic *Pnma* phase, feature average fourfold cation coordination, because one cation has threefold coordination and the other has fivefold coordination. Therefore, they show intermediate cation coordination between the threefold coordination of α-As$_2$S$_3$ and the sixfold coordination of α-Sb$_2$Te$_3$. They exhibit softening of some high-frequency modes.[50–52] In particular, softening of two high-frequency modes has been observed in α-Sb$_2$S$_3$ up to 12 GPa, a pressure at which Sb1 and Sb2 can be considered to have almost sevenfold coordination due to pressure-induced metavalent bonding of both Sb atoms.[52] These compounds have been recently shown not to be metavalent at room pressure,[81] becoming metavalent at HP according to our work.

An intermediate case between covalent and metavalent bonding is also that of α-As$_2$Te$_3$, which shows an average cation coordination of 5.5, because one cation has 3 + 2 coordination and the other has 3 + 3 coordination. Therefore, it shows intermediate coordination between the fivefold coordination of α-Sb$_2$Se$_3$ and the sixfold coordination of α-Sb$_2$Te$_3$. Consequently, α-As$_2$Te$_3$ shows almost no soft phonons. Only a few high-frequency phonons show soft behavior with an almost negligible pressure coefficient between 0 and 4 GPa and a notable hardening above this pressure.[53] An inspection of the evolution of the As–Te distances in this pressure range shows that the As1 (As2) coordination changes from almost five (six) at room pressure to real six (six) above 4 GPa. Therefore, the changes observed in the pressure coefficients of the zone-center vibrational modes in α-As$_2$Te$_3$ are indicative of a change of bonding type from almost metavalent bonding inside the layers to full metavalent bonding that takes into account also interactions between the layers. Finally, β-As$_2$Te$_3$ with $R\bar{3}m$ symmetry and sixfold coordination has been confirmed to show metavalent bonding[81] and is expected to show no soft modes like α-Bi$_2$Se$_3$, α-Bi$_2$Te$_3$ and α-Sb$_2$Te$_3$.[67]

It must be noted that a notable decrease of the bandgap with pressure has also been obtained in DFT calculations for α-Sb$_2$S$_3$, α-Sb$_2$Se$_3$ and α-Bi$_2$S$_3$,[52] and at a smaller rate also for α-As$_2$Te$_3$[67] and Bi$_2$Te$_3$.[82] In fact, we have observed metallization around 26 GPa in our DFT calculations for α-As$_2$S$_3$, similar to the metallization found around 4 GPa for α-As$_2$Te$_3$ and above 12 GPa for α-Sb$_2$S$_3$. Therefore, it is expected that a similar increase of the dielectric tensors and the Born effective charges at HP occurs in these group-15 sesquichalcogenides, thus supporting the occurrence of metavalent bonding in these compounds at HP.

C Experimental and theoretical description

C.1 Experimental details

Almost pure mineral orpiment from Hunan province (China) was used in the present study. Angle-dispersive powder HP-XRD experiments at room temperature up to 25 GPa were conducted in a membrane-type diamond anvil cell (DAC) at the BL04-MSPD beamline of the ALBA synchrotron. The incident monochromatic beam with a wavelength of 0.4246 Å was focused to 20 × 20 μm^2 using a pinhole of 50 μm to cut the X-ray beam tail.[83] Images covering a 2θ range up to 18° were collected using a SX165 CCD located at 240 mm from the sample. One-dimensional diffraction profiles of intensity as a function of 2θ were obtained by integration of the observed intensities with the Fit2D software.[84] Le Bail refinements were carried out with the GSAS software package for synchrotron measurements.[85,86] Interatomic distances were obtained with the Visualization for Electronic and Structural Analysis (VESTA) software.[87] The EoS of copper,[88] which was mixed with the sample powder, was used for pressure calibration.

Room-temperature unpolarized HP-RS measurements up to 14.5 GPa were carried out with a Horiba Jobin Yvon LabRAM HR spectrometer equipped with a thermoelectrically cooled

This journal is © the Owner Societies 2020

Phys. Chem. Chem. Phys., 2020, **22**, 3352–3369 | **3365**

multichannel CCD detector. RS measurements with a spectral resolution better than 2 cm^{-1} were performed using the 632.8 nm line of a He:Ne laser with a power below 1 mW in order to avoid laser heating of the sample. The use of an edge filter limited the observation of Raman-active modes below 40 cm^{-1}. The pressure was determined with the ruby fluorescence method.[89] In both HP-XRD and HP-RS measurements, a methanol–ethanol (4:1 ratio) mixture was used as a pressure-transmitting medium with quasi-hydrostatic conditions up to 10 GPa and the deviatoric stresses are within the experimental uncertainty of this soft material up to 25 GPa.[90,91]

C.2 Theoretical details

Ab initio calculations within DFT[92] were performed to compute the electronic and structural properties of α-As$_2$S$_3$ by using the plane-wave Vienna Ab initio Simulation Package (VASP).[93,94] The projector-augmented wave scheme (PAW)[95] was considered to treat the valence and the semi-core states more explicitly by including the 4s and 4p outermost electrons of As and the 3s and 3p electrons of S as valence electrons, with the remaining electrons being considered frozen at the core. In this work, the generalized gradient approximation with the Perdew–Burke–Ernzerhof (PBE)[96] parametrization was used for the exchange and correlation energy, after evaluating calculations performed also with the PBEsol modified version[97] in ref. 35. The plane-wave kinetic-energy cutoff was defined as 360 eV, which together with the use of a dense Monkhorst–Pack grid[98] with a 6 × 4 × 2 *k*-point reciprocal space sampling mesh ensured a convergence of the total energy of around 1 meV with deviations of the stress tensor from a diagonal hydrostatic form of less than 1 kbar (0.1 GPa). The vdW corrections to the total energy were taken into account within DFT by using the D2 method.[99] Electronic band-structure calculations were carried out at different pressures along selected high-symmetry *k*-points on the first BZ. Additionally, analysis of the electron density topology and of the ELF was accomplished with the VESTA program employing data from the VASP code.[100,101]

Lattice-dynamics calculations were performed at the zone center (Γ-point) and along high-symmetry segments of the BZ as a function of pressure, by using the direct-force constant approach.[102,103] The separate calculations of the forces which result from a fixed displacement away from equilibrium of the atoms in the primitive cell necessary for the construction of the dynamical matrix at the Γ-point of the BZ were achieved with VASP. The diagonalization of the dynamical matrix provides the normal-mode frequencies and allows identifying the irreducible representations and the character of the vibrational phonon modes at the Γ-point.

D Conclusions

The monoclinic structure of orpiment (α-As$_2$S$_3$) at room conditions is composed of layers formed by AsS spiral chains, where the As atoms have threefold coordination. We have studied the structural, vibrational, and electronic properties of orpiment at room temperature and HP and have found that orpiment undergoes strong compression up to 20 GPa, followed by an IPT of electronic origin, which leads to a coordination of As which is higher than five above that pressure. The most striking feature of the pressure-induced IPT is that several As–S bond distances become equal above 20 GPa.

The lattice dynamics of orpiment has been studied and all the rigid layer modes and the main inter-chain and intra-chain modes have been fully described. Our measurements and calculations evidence the softening of many vibrational modes and the decrease of the phonon gap (it closes above 20 GPa) at HP. Moreover, our calculations confirm the metallization of orpiment above 26 GPa due to the strong decrease of the optical bandgap, thus supporting metallization in the laboratory under hydrostatic conditions well above 50 GPa when taking into consideration the underestimation of the energy bandgap in DFT calculations. All these changes are related to the formation of metavalent bonding occurring in orpiment above 20 GPa due to the delocalization of electronic clouds, mainly in the *ac*-plane of the layers, leading to an increase of cation coordination (more than fivefold) without the need for a first-order structural phase transition as in Se and Te, and similar to GeSe upon the *Pnma* to *Cmcm* phase transition.[43]

On top of that, we have suggested that metavalent bonding already occurs in other group-15 sesquichalcogenides at room pressure or at HP. Full metavalent bonding occurs in topological insulators and good thermoelectric materials such as α-Bi$_2$Se$_3$, α-Bi$_2$Te$_3$ and α-Sb$_2$Te$_3$ with tetradymite layered structure that feature sixfold cation coordination. In these compounds, transformation from metavalent to metallic bonding occurs at HP (still not proved for β-As$_2$Te$_3$) after a first-order phase transition to a structure with cation coordination larger than the original sixfold-coordinated one. On the other hand, partial metavalent bonding occurs in α-Bi$_2$S$_3$, α-Sb$_2$S$_3$ and α-Sb$_2$Se$_3$, with an orthorhombic *Pnma* structure, and in α-As$_2$Te$_3$. These compounds show intermediate coordination between three and six. In all these compounds, pressure increases the cation coordination, leading to a considerable bandgap reduction and partial phonon softening consistent with metavalent bonding at HP. Finally, we predict that a similar situation to that for As$_2$S$_3$ is expected for As$_2$Se$_3$ polymorphs and also in the low-pressure trigonal Se and Te at HP. These compounds featuring threefold coordination at room pressure are expected to exhibit metavalent bonding at HP.

In summary, our present results on α-As$_2$S$_3$ confirm that pressure is able to tune the metavalent bonding in group-15 sesquichalcogenides, such as occurs for orpiment, thus turning common semiconductors into "incipient metals" with promising phase-change, thermoelectric and topological insulating properties at extreme conditions. Since Sb$_2$Te$_3$ and Bi$_2$Te$_3$ are topological insulators and two of the best known thermoelectric materials at room conditions due to metavalent bonding,[81] this work paves the way to design new group-15 sesquichalcogenides and related compounds with thermoelectric or topological insulating properties both at room pressure and at extreme conditions.

3366 | *Phys. Chem. Chem. Phys.*, 2020, **22**, 3352–3369

This journal is © the Owner Societies 2020

Conflicts of interest

There are no conflicts to declare.

Acknowledgements

Notes and references

1 J. D. Smith, J. C. Bailar, H. J. Emeléus and R. Nyholm, The Chemistry of Arsenic, Antimony and Bismuth, *Pergamon Texts in Inorganic Chemistry*, 1973, vol. 2.
2 *Pliny the Elder, Naturalis Historia*, ed. J. Bostock and H. T. Riley, Taylor and Francis, London, 1855, ch. 22.
3 E. W. Fitzhugh, Orpiment and Realgar, in Artists' Pigments, *A Handbook of Their History and Characteristics*, Oxford University Press, 1997, vol. 3, pp. 47–80.
4 F. C. J. Spurrell, *Archaeol. J.*, 1895, **52**, 222–239.
5 L. Burgio and R. J. H. Clark, *J. Raman Spectrosc.*, 2000, **31**, 395–401.
6 S. Waxman and K. C. Anderson, *Oncologist*, 2001, **6**(Suppl 2), 3–10.
7 W. Ding, Y. Tong, X. Zhang, M. Pan and S. Chen, *Sci. Rep.*, 2016, **6**, 19793.
8 J. Heo and W. J. Chung, Rare-earth-doped chalcogenide glass for lasers and amplifiers, *Chalcogenide Glasses: Preparation, Properties and Applications*, Woodhead Publishing, 2014, pp. 347–380.
9 D. W. Hewak, N. I. Zheludev and K. F. MacDonald, Controlling light on the nanoscale with chalcogenide thin films, *Chalcogenide Glasses: Preparation, Properties and Applications*, Woodhead Publishing, 2014, pp. 471–508.
10 N. Morimoto, *Mineral. J.*, 1954, **1**, 160–169.
11 D. J. E. Mullen and W. Nowacki, *Z. Kristallogr.*, 1972, **136**, 48–65.
12 A. R. Kampf, R. T. Downs, R. M. Housley, R. A. Jenkins and J. Hyršl, *Mineral. Mag.*, 2011, **75**, 2857–2867.
13 G. V. Gibbs, A. F. Wallace, R. Zallen, R. T. Downs, N. L. Ross, D. F. Cox and K. M. Rosso, *J. Phys. Chem. A*, 2010, **114**, 6550–6557.
14 H. F. Cheng, Y. Zhou and R. L. Frost, *Spectrosc. Lett.*, 2017, **50**, 23–29.
15 S. P. S. Porto and D. L. Wood, *J. Opt. Soc. Am.*, 1962, **52**, 251–252.
16 A. Weber and S. P. S. Porto, *J. Opt. Soc. Am.*, 1965, **55**, 1033–1034.
17 A. T. Ward, *J. Phys. Chem.*, 1968, **72**, 4133–4139.
18 R. Forneris, *Am. Mineral.*, 1969, **54**, 1062–1074.
19 W. Scheuermann and G. J. Ritter, *Z. Naturforsch.*, 1969, **A24**, 408–411.
20 J. M. Mathieu and H. Poulet, *Bull. Soc. Fr. Mineral. Cristallogr.*, 1970, **93**, 532–535.
21 R. Zallen, M. Slade and A. T. Ward, *Phys. Rev. B: Solid State*, 1971, **3**, 4257–4273.
22 R. Zallen and M. Slade, *Phys. Rev. B: Solid State*, 1974, **9**, 1627–1637.
23 R. Zallen, *Phys. Rev. B: Solid State*, 1974, **9**, 4485–4496.
24 A. P. DeFonzo and J. Tauc, *Phys. Rev. B: Solid State*, 1978, **18**, 6957–6972.
25 C. Razzetti and P. P. Lottici, *Solid State Commun.*, 1979, **29**, 361–364.
26 J. M. Besson, J. Cernogora and R. Zallen, *Phys. Rev. B: Condens. Matter Mater. Phys.*, 1980, **22**, 3866–3876.
27 J. M. Besson, J. Cernogora, M. L. Slade, B. A. Weinstein and R. Zallen, *Phys. B*, 1981, **105**, 319–323.
28 R. L. Frost, W. N. Martens and J. T. Kloprogge, *Neues Jahrb. Mineral., Monatsh.*, 2002, **10**, 469–480.
29 S. Mamedov and N. Drichko, *MRS Adv.*, 2018, **3**, 385–390.
30 J. P. Itié, A. Polian, M. Grimsditch and S. Susman, *Jpn. J. Appl. Phys.*, 1992, **32**, 719–721.
31 R. Zallen, *High Pressure Res.*, 2004, **24**, 117–118.
32 N. B. Bolotina, V. V. Brazhkin, T. I. Dyuzheva, Y. Katayama, L. F. Kulikova, L. V. Lityagina and N. A. Nikolaev, *JETP Lett.*, 2013, **98**, 539–543.
33 K. X. Liu, L. D. Dai, H. P. Li, H. Y. Hu, L. F. Yang, C. Pu, M. L. Hong and P. F. Liu, *Materials*, 2019, **12**, 784.
34 E. A. Kravchenko, A. V. Timofeeva and G. Z. Virogradova, *J. Mol. Struct.*, 1980, **58**, 253–262.
35 S. Radescu, A. Mujica, P. Rodríguez-Hernández, A. Muñoz, J. Ibáñez, J. A. Sans, V. P. Cuenca-Gotor and F. J. Manjón, *J. Phys.: Conf. Ser.*, 2017, **950**, 042018.
36 M. Šiškins, M. Lee, F. Alijani, M. R. van Blankenstein, D. Davidovikj, H. S. J. van der Zant and P. G. Steeneken, *ACS Nano*, 2019, **13**, 10845–10851.
37 Z. Bao and X. D. Chen, *Adv. Mater.*, 2016, **28**, 4177–4179.
38 J. H. Koo, D. C. Kim, H. J. Shim, T.-H. Kim and D.-H. Kim, *Adv. Funct. Mater.*, 2018, **28**, 1801834.
39 M. A. García-Bucio, M. Á. Maynez-Rojas, E. Casanova-González, J. J. Cárcamo-Vega, J. L. Ruvalcaba-Sil and A. Mitrani, *J. Raman Spectrosc.*, 2019, **50**, 1546–1554.
40 K. Shportko, S. Kremers, M. Woda, D. Lencer, J. Robertson and M. Wuttig, *Nat. Mater.*, 2008, **7**, 653–658.
41 S. Lee, K. Esfarjani, T. F. Luo, J. W. Zhou, Z. T. Tian and G. Chen, *Nat. Commun.*, 2014, **5**, 3525.
42 C. W. Li, J. Hong, A. F. May, D. Bansal, S. Chi, T. Hong, G. Ehlers and O. Delaire, *Nat. Phys.*, 2015, **11**, 1063–1069.

This journal is © the Owner Societies 2020

Phys. Chem. Chem. Phys., 2020, **22**, 3352–3369 | **3367**

43 M. Xu, S. Jakobs, R. Mazzarello, J.-Y. Cho, Z. Yang, H. Hollermann, D. S. Shang, X. S. Miao, Z. H. Yu, L. Wang and M. Wuttig, *J. Phys. Chem. C*, 2017, **121**, 25447–25454.

44 M. Wuttig, W. L. Deriger, X. Gonze, C. Bichara and J.-Y. Raty, *Adv. Mater.*, 2018, **30**, 1803777.

45 J.-Y. Raty, M. Schumacher, P. Golub, V. L. Deringer, C. Gatti and M. Wuttig, *Adv. Mater.*, 2018, **31**, 1806280.

46 C. Svensson, *Acta Crystallogr., Sect. B: Struct. Crystallogr. Cryst. Chem.*, 1974, **30**, 458–461.

47 A. C. Stergiou and P. J. Rentzeperis, *Z. Kristallogr.*, 1985, **173**, 185–191.

48 F. Pertlik, *Monatsh. Chem.*, 1978, **109**, 277–282.

49 A. Brown and S. Rundqvist, *Acta Crystallogr.*, 1965, **19**, 684–685.

50 I. Efthimiopoulos, J. M. Zhang, M. Kucway, C. Y. Park, R. C. Ewing and Y. Wang, *Sci. Rep.*, 2013, **3**, 2665–2672.

51 I. Efthimiopoulos, J. Kemichick, X. Zhou, S. V. Khare, D. Ikuta and Y. Wang, *J. Phys. Chem. A*, 2014, **118**, 1713–1720.

52 J. Ibañez, J. A. Sans, C. Popescu, J. López-Vidrier, J. J. Elvira-Betanzos, V. P. Cuenca-Gotor, O. Gomis, F. J. Manjón, P. Rodríguez-Hernández and A. Muñoz, *J. Phys. Chem. C*, 2016, **120**, 10547–10558.

53 V. P. Cuenca-Gotor, J. A. Sans, J. Ibáñez, C. Popescu, O. Gomis, R. Vilaplana, F. J. Manjón, A. Leonardo, E. Sagasta, A. Suárez-Alcubilla, I. G. Gurtubay, M. Mollar and A. Bergara, *J. Phys. Chem. C*, 2016, **120**, 19340–19352.

54 A. Walsh, D. J. Payne, R. G. Egdell and G. W. Watson, *Chem. Soc. Rev.*, 2011, **40**, 4455–4463.

55 P. Srivastava, H. Singh Mund and Y. Sharma, *Phys. B*, 2011, **406**, 3083–3088.

56 E. Kroumova, M. I. Arroyo, J. M. Perez-Mato, A. Kirov, C. Capillas, S. Ivantchev and H. Wondratschek, *Phase Transitions*, 2003, **76**, 155–170.

57 P. Canepa, R. M. Hanson, P. Ugliengo and M. Alfredsson, *J. Appl. Crystallogr.*, 2011, **44**, 225–229.

58 H. Siebert, *Z. Anorg. Allg. Chem.*, 1954, **275**, 225–240.

59 F. Birch, *J. Appl. Phys.*, 1938, **9**, 279–288.

60 P. A. Guńka, M. Dranka, M. Hanfland, K. F. Dziubek, A. Katrusiak and J. Zachara, *Cryst. Growth Des.*, 2015, **15**, 3950–3954.

61 S. Haussühl, *Physical Properties of Crystals. An Introduction*, Wiley-VCH, 2007.

62 R. J. Angel, 2019, http://www.rossangel.com/text_strain.htm.

63 S. Minomura, K. Aoki, N. Koshizuka and T. Tsushima, *High-Pressure Science and Technology*, Springer, 1979, p. 435.

64 A. K. Bandyophadhay and D. B. Singh, *Pramana*, 1999, **52**, 303–319.

65 Y. A. Sorb, V. Rajaji, P. S. Malavi, U. Subbarao, P. Halappa, S. C. Peter, S. Karmakar and C. Narayana, *J. Phys.: Condens. Matter*, 2016, **28**, 015602.

66 I. Efthimiopoulos, C. Buchan and Y. Wang, *Sci. Rep.*, 2016, **6**, 24246.

67 F. J. Manjón, R. Vilaplana, O. Gomis, E. Perez-Gonzalez, D. Santamaria-Perez, V. Marin-Borras, A. Segura, J. Gonzalez, P. Rodriguez-Hernandez and A. Muñoz, *Phys. Status Solidi B*, 2013, **250**, 669–676.

68 J. A. Sans, F. J. Manjón, A. L. J. Pereira, R. Vilaplana, O. Gomis, A. Segura, A. Muñoz, P. Rodríguez-Hernández, C. Popescu, C. Drasar and P. Ruleova, *Phys. Rev. B*, 2016, **93**, 024110.

69 A. L. J. Pereira, D. Santamaría-Pérez, J. Ruiz-Fuertes, F. J. Manjón, V. P. Cuenca-Gotor, R. Vilaplana, O. Gomis, C. Popescu, A. Muñoz, P. Rodríguez-Hernández, A. Segura, L. Gracia, A. Beltrán, P. Ruleova, C. Drasar and J. A. Sans, *J. Phys. Chem. C*, 2018, **122**, 8853–8867.

70 O. Degtyareva, E. R. Hernández, J. Serrano, M. Somayazulu, H.-K. Mao, E. Gregoryanz and R. J. Hemley, *J. Chem. Phys.*, 2007, **126**, 084503.

71 W. Richter, J. B. Renucci and M. Cardona, *Phys. Status Solidi B*, 1973, **56**, 223–229.

72 K. Aoki, O. Shimomura, S. Minomura, N. Koshizuka and T. Tsushima, *J. Phys. Soc. Jpn.*, 1980, **48**, 906–911.

73 G. Lucogsky, *Phys. Status Solidi B*, 1972, **49**, 633–641.

74 I. M. Lifshitz, *Sov. Phys. - JETP*, 1960, **11**, 1130.

75 I. D. Brown, *Acta Crystallogr., Sect. B: Struct. Sci.*, 1988, **44**, 545–553.

76 M. Dudev, J. Wang, T. Dudev and C. Lim, *J. Phys. Chem. B*, 2006, **110**, 1889–1895.

77 I. D. Brown, *Am. Mineral.*, 2016, **101**, 531–539.

78 No value is obtained at higher pressure since the metallization of the monoclinic structure above 25 GPa in our calculations yields unreasonably high values of these parameters.

79 L. Properzi, A. Polian, P. Munsch and A. Di Cicco, *High Press. Res.*, 2013, **33**, 35–39.

80 C. Marini, D. Chermisi, M. Lavagnini, D. Di Castro, C. Petrillo, L. Degiorgi, S. Scandolo and P. Postorino, *Phys. Rev. B: Condens. Matter Mater. Phys.*, 2012, **86**, 064103.

81 Y. Chen, O. Cojocaru-Mirédin, J. Keutgen, Y. Yu, M. Küpers, M. Shumacher, P. Golub, J.-Y. Raty, R. Dronskowski and M. Wuttig, *Adv. Mater.*, 2019, **31**, 1904316.

82 R. Vilaplana, O. Gomis, F. J. Manjón, A. Segura, E. Pérez-González, P. Rodríguez-Hernández, A. Muñoz, J. González, V. Marín-Borrás, V. Muñoz-Sanjosé, C. Drasar and V. Kucek, *Phys. Rev. B: Condens. Matter Mater. Phys.*, 2011, **84**, 104112.

83 F. Fauth, I. Peral, C. Popescu and M. Knapp, *Powder Diffr.*, 2013, **28**, S360–S370.

84 A. P. Hammersley, S. O. Svensson, M. Hanfland, A. N. Fitch and D. Hausermann, *High Press. Res.*, 1996, **14**, 235–248.

85 A. C. Larson and R. B. von Dreele, *Los Alamos Sci. Lab. Rep.*, 2004, **86**, 748.

86 B. H. Toby, *J. Appl. Crystallogr.*, 2001, **34**, 210–213.

87 K. Momma and F. Izumi, *J. Appl. Crystallogr.*, 2011, **44**, 1272–1276.

88 A. Dewaele, P. Loubeyre and M. Mezouar, *Phys. Rev. B: Condens. Matter Mater. Phys.*, 2004, **70**, 094112.

89 H. K. Mao, J. Xu and P. M. Bell, *J. Geophys. Res.*, 1986, **91**, 4673–4676.

90 G. J. Piermarini, S. Block and J. D. Barnett, *J. Appl. Phys.*, 1973, **44**, 5377–5382.

91 S. Klotz, J.-C. Chervin, P. Munsch and G. Le Marchand, *J. Phys. D: Appl. Phys.*, 2009, **42**, 075413.

92 P. Hohenberg and W. Kohn, *Phys. Rev.*, 1964, **136**, B864–B871.

93 G. Kresse and J. Hafner, *Phys. Rev. B: Condens. Matter Mater. Phys.*, 1993, **47**, 558–561.

94 G. Kresse and J. Furthmüller, *Comput. Mater. Sci.*, 1996, **6**, 15–50.

95 P. E. Blöchl, *Phys. Rev. B: Condens. Matter Mater. Phys.*, 1994, **50**, 17953–17979.

96 J. P. Perdew, K. Burke and M. Ernzerhof, *Phys. Rev. Lett.*, 1996, **77**, 3865–3868.

97 J. P. Perdew, A. Ruzsinszky, G. I. Csonka, O. A. Vydrov, G. E. Scuseria, L. A. Constantin, X. Zhou and K. Burke, *Phys. Rev. Lett.*, 2008, **100**, 136406.

98 H. J. Monkhorst and J. D. Pack, *Phys. Rev. B: Solid State*, 1976, **13**, 5188–5192.

99 S. Grimme, *J. Comput. Chem.*, 2006, **27**, 1787–1799.

100 J. Contreras-García, A. Martin Pendás, B. Silvi and J. M. Recio, *J. Phys. Chem. Solids*, 2008, **69**, 2204–2207.

101 J. Contreras-García, B. Silvi, A. Martín Pendás and J. M. Recio, *J. Chem. Theory Comput.*, 2009, **5**, 164–173.

102 K. Parlinski, Z. Q. Li and Y. Kawazoe, *Phys. Rev. Lett.*, 1997, **78**, 4063–4066.

103 D. Alfè, *Comput. Phys. Commun.*, 2009, **180**, 2622–2633.